



**DEVELOPMENT AND DEMONSTRATION
OF A FIELD-DEPLOYABLE FAST
CHROMOTOMOGRAPHIC IMAGER**

THESIS

Daniel O'Dell, Captain, USAF
AFIT/GEO/ENP/10-M01

**DEPARTMENT OF THE AIR FORCE
AIR UNIVERSITY**

AIR FORCE INSTITUTE OF TECHNOLOGY

Wright-Patterson Air Force Base, Ohio

APPROVED FOR PUBLIC RELEASE; DISTRIBUTION UNLIMITED.

The views expressed in this thesis are those of the author and do not reflect the official policy or position of the United States Air Force, Department of Defense, or the United States Government.

AFIT/GEO/ENP/10-M01

DEVELOPMENT AND DEMONSTRATION OF A FIELD-DEPLOYABLE FAST
CHROMOTOMOGRAPHIC IMAGER

THESIS

Presented to the Faculty
Department of Electrical and Computer Engineering
Graduate School of Engineering and Management
Air Force Institute of Technology
Air University
Air Education and Training Command
in Partial Fulfillment of the Requirements for the
Degree of Master of Science in Electrical Engineering

Daniel O'Dell, BSME
Captain, USAF

March 2010

APPROVED FOR PUBLIC RELEASE; DISTRIBUTION UNLIMITED.

AFIT/GEO/ENP/10-M01

DEVELOPMENT AND DEMONSTRATION OF A FIELD-DEPLOYABLE FAST
CHROMOTOMOGRAPHIC IMAGER

Daniel O'Dell, BSME
Captain, USAF

Approved:

//signed//

March 2010

Lt Col Michael R. Hawks (Chairman)

Date

//signed//

March 2010

Glen P. Perram PhD (Member)

Date

//signed//

March 2010

Lt Col Eric D. Swenson (Member)

Date

Abstract

A field deployable hyperspectral imager utilizing chromotomography (CT), with a direct vision prism (DVP) as the dispersive element, has been constructed at AFIT. This research is focused on the development and demonstration of the CT imager. An overview of hyperspectral imaging, chromotomography, a synopsis of reconstruction algorithms, and other CT instruments are given. The importance of component alignment, instrument calibration, and exact prism angular position data are discussed. A simplistic “shift and add” reconstruction algorithm was utilized for this research. Although limited in its ability to reconstruct a spatially and spectrally diverse scene, the algorithm was adequate for the testing and characterization of the CT imager. The AFIT instrument is currently the fastest known DVP based hyperspectral CT imager and is a prototype for a planned space-based system. The instrument has the ability to capture spatial and spectral data of static and transient scenes. Spectral and spatial reconstructions of static scenes are presented in the Experimental Results and Analysis section of this paper. These reconstructions illustrate the effectiveness of the instrument to collect spatial and spectral data. More importantly, the imager can capture spectral data of rapidly evolving scenes such as explosions. The spectrum of a transient event, a firecracker explosion, lasting approximately 0.12 s is presented. Spectral results of the explosion show potassium and sodium emission lines present during the explosion and an absorption feature as the fireball extinguishes. Spatial and spectral reconstruction of a scene in which an explosion occurs during the middle of the collection period is also presented in the Experimental Results and Analysis section of this paper.

Acknowledgements

I would like to thank Lt Col Hawks, my advisor, who was always willing to assist me in completing my research. He is the best advisor a student could ask for. I cannot say enough good things about him.

Additionally, I'd like to thank the other members of my committee, Dr. Perram and Lt Col Swenson. Dr. Perram first involved me in this project and provided wonderful insight and guidance throughout my time at AFIT. Lt Col Swenson, who like me started his officer career in civil engineering, was a great mentor and always asked the right questions to keep me thinking.

As with any research there were numerous others who guided and assisted me. First and foremost was Randy Bostick. His doctoral work was the basis of much of my research. He continually assisted me in my work and greatly eased many challenges in my research with his expertise. My brother and my close friend R. S. have earned my gratitude for reviewing my paper and making it better. I would also like to thank the laboratory technicians; Greg Smith, Sean Miller, Ben Schott, Jeremy Pitz and Mike Ranft; and the other students and faculty involved in CTE_x and my research; Doug McDonald, Dr. Cobb, Dr. Black, MAJ Book, Art Morse, and Steve Miller. They assisted in all stages of my research and made a huge project very manageable and successful.

Finally, I couldn't have completed my degree and thesis without the support of my loving family. I am eternally indebted to my wonderful wife and the love of my life, and my two beautiful children. They mean the world to me.

Daniel O'Dell

Table of Contents

	Page
Abstract	iv
Acknowledgements	v
List of Figures	viii
List of Tables	xi
I. Introduction	1
1.1 Hyperspectral Imaging Background	1
1.2 Current and Previous Chromotomographic Systems	8
1.2.1 Non-Prism CT Systems	8
1.2.2 Prism-based CT Systems	9
1.3 Organization of Thesis	11
II. Theory of Prism-Based Chromotomographic Imagers	12
2.1 Chromotomography's link to X-Ray Tomography	12
2.2 Typical Components of CT Imagers	13
2.3 Advantages of Prism-based CT Imagers	14
2.4 Dispersion of Prisms	14
III. Instrument Description and Experimental Procedures	17
3.1 Instrument Description	17
3.2 Experimental Procedures	22
IV. Data Acquisition and Algorithm Development	24
4.1 Data Acquisition	24
4.2 Reconstruction Algorithm	30
4.2.1 Algorithm Background	30
4.2.2 Algorithm Description	31
V. Experimental Results and Analysis	44
5.1 Algorithm and Instrument Performance	44
5.2 An Extended Scene, Broadband Spectrum	53
5.3 Transient Event Reconstruction	64

	Page
VI. Conclusions and Recommendations	74
Bibliography	76

List of Figures

Figure		Page
1	AVIRIS hyperspectral data cube	2
2	An example of a grating	4
3	An example of a dispersive spectrometer.	5
4	An example of an interferometer.	5
5	An example of an interference pattern created by an interferometer. . .	6
6	An example of a push broom hyperspectral sensor.	6
7	A typical layout of a CT instrument.	13
8	Drawing of the prisms utilized in the CT imager.	15
9	A graphical representation of dispersion in a prism.	15
10	Theoretical and actual dispersion of prism	15
11	Picture of AFIT CT imager	18
12	Sketch of AFIT CT imager	18
13	Spectral response for the Phantom v5.1 camera	21
14	Hg point source	26
15	Hg dispersion through DVP	26
16	Dispersed image of a resolution chart	27
17	T-22 USAF resolution chart	27
18	Notional dispersion of a resolution chart	28
19	Overfilled FPA	29
20	Prism transverse shift	32
21	Prism “offset ring” image	34
22	“Offset ring” location plot	34

Figure		Page
23	A composite image of different pen lamps.	35
24	Plots of pixel and offset ring displacement	38
25	Notional “shift and add” reconstruction of a resolution chart	39
26	Reconstructed image at an emitted spectral line	40
27	An “off-wavelength” reconstructed image	40
28	On-wavelength processed images of a resolution chart	42
29	Off-wavelength processed image of a resolution chart	42
30	A plot of the intensity of reconstructed bins	43
31	Reconstruction of a point-like source utilizing estimated position	45
32	Reconstruction of a point-like source utilizing centroid position	47
33	A logarithmic scaled reconstruction of a point-like source utilizing centroid position	47
34	A plot of the actual and estimated location of a point-like source	48
35	A plot of the difference between actual and estimated point-like source locations	49
36	A line width comparison of the “precise” and “estimated” reconstructed images	50
37	Comparison of lab and field alignment	52
38	The reconstructed intensity image of a point-like source at 436 nm, 546 nm, and 635 nm	54
39	Reconstructed intensity images for a Hg point-like source ranging from 440 to 550 nm	55
40	Raw image and intensity image of an American flag	56

Figure		Page
43	Picture of the flag without the prism in place and Bostick's reconstructed image of the flag	62
44	Spectral plots of different parts of Bostick's reconstructed American flag	63
45	Unprocessed images of a transient event	65
46	The reconstructed image at 568 nm of a Hg pen lamp after a transient event	65
47	Closeup reconstructed images a Hg pen light at 568 nm, 546 nm, 436 nm	67
48	Images of the box that housed the Hg pen light during the transient tests	67
49	Intensity image and spectral plot of a firecracker detonation	68
50	Intensity plot of entire explosion	70
51	Intensity plots of explosion up to $t=0.004$ s	71
52	Plot of potassium, sodium, and absorption bands	72
53	An AFIT sign illuminated by an explosion	73

List of Tables

Table		Page
1	Phantom v5.1 maximum fps	21
2	Observed spectral lines with deviation from un-dispersed wavelength.	34
3	Best fit parameters for the model.	36
4	Wavelength dispersion in constant pixel increments.	59
5	Pixel displacement in constant wavelength increments.	59

DEVELOPMENT AND DEMONSTRATION OF A FIELD-DEPLOYABLE FAST CHROMOTOMOGRAPHIC IMAGER

I. Introduction

The Air Force Institute of Technology (AFIT) is developing a space-based chromotomographic (CT) hyperspectral imager to be placed on the International Space Station (ISS). Because CT imaging has the potential ability to capture spatial and spectral data from transient events, a space-based system may enhance current capabilities of identifying, classifying, and characterizing battlespace events such as artillery/AAA muzzle flashes, detonations, and missile launches. Previous AFIT CT research has mainly focused on algorithm development, theoretical comparison of differing CT systems, and analysis of laboratory based systems [3; 18; 19; 20; 23; 24; 31]. The concept for a space-based system evolved from Bostick's laboratory work on the development and characterization of a CT instrument utilizing a direct vision prism (DVP) [3]. The first DVP based CT imagers were created more than a decade ago by Mooney et. al. [27]. A few other laboratory based CT imagers, of varying types, have been manufactured over the past ten years [17; 28]; however, most of these systems are not well characterized in literature. Developing and demonstrating a field deployable CT hyperspectral imager is the focus of this thesis and is the next logical step in the creation of a space-based imager.

1.1 Hyperspectral Imaging Background

CT imagers operate on many of the same basic principles that were utilized in developing hyperspectral sensing, spectrometers, and imaging spectrometers. Therefore

a brief discussion of these systems facilitates the understanding of CT instruments.

Traditional imaging methods typically capture two spatial dimensions of a scene over a broad spectral range, such as the visible spectrum, or over a narrow spectral range, such as imaging a scene with a bandpass filter. Hyperspectral imaging’s advantage over many traditional sensing methods is that it collects data in tens to hundreds of separate narrow spectral bands over the same two dimensional spatial plane as traditional imaging methods.

Processing of the hyperspectral instrument’s captured data of a scene creates a three dimensional image cube, also referred to as a “data cube.” As illustrated in Figure 1, two of the dimensions of the data cube are spatial, the x and y axes, and the third dimension, the z axis, is composed of the spectral data collected. A “slice” parallel to the z axis would produce a two dimensional spatial image of a scene at a particular spectral band. The “slice” is equivalent to imaging a scene with a bandpass filter. A plot of the intensities of a particular x and y coordinate of the data cube in the z direction would produce a spectral plot of that coordinate. From analyses of the captured data, information such as the chemical composition of the scene and atmospheric phenomena may be determined. The data from hyperspectral sensing is utilized for various applications, such as vegetation management, atmospheric monitoring of pollutants, and military monitoring of battlefield activity [8]. To derive the

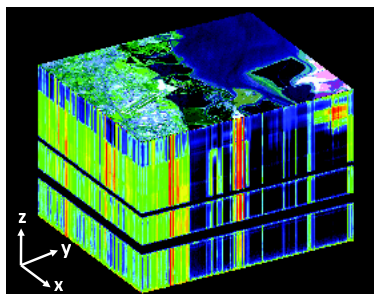


Figure 1. AVIRIS hyperspectral data cube over Moffett Field, CA. The two spatial dimensions are the x and y axes and the z axis represents the spectral dimension. Image courtesy of the Jet Propulsion Laboratory, Pasadena California [22].

spectral data from a scene, hyperspectral imagers utilize the wave nature of light to separate broadband light into spectral bands.

Refraction, interference, and diffraction of light are utilized separately or in combination to separate broadband light into spectral bands, a process referred to as dispersion. Refraction describes the change of light’s path traveling from one medium, such as air, into another medium, such as glass. The index of refraction describes the speed with which light travels through a medium. For most mediums the index of refraction is wavelength dependent, denoted as $n(\lambda)$. In other words, differing wavelengths of a light travels at different rates through a medium. Diffraction describes how every point of a wavefront acts as a source of waves, allowing light to “bend” around obstacles. Interference describes the effect of two light waves combining to cancel or reinforce each other. Spectrometers were some of the first instruments to utilize the wave nature of light and observe spectral features of objects.

There are two main classes of spectrometers. The first type utilizes dispersive elements, such as diffraction gratings and prisms, to separate the emitted light into specific wavelengths. For grating based instruments, dispersion is caused by diffraction and interference [35]. Figure 2 is an example of how a grating disperses light. For prism based instruments, dispersion occurs because the index of refraction is wavelength dependent [21]. A classic example of the wavelength dependance of refraction is when white light strikes a prism and creates the visible light spectrum, e.g. a rainbow. The following equation is utilized to calculate the index of refraction, or refractive index, for a material.

$$n(\lambda) = \frac{c}{v} \tag{1}$$

where n is the index of refraction, c is the velocity of the light wave phenomenon, and v is the phase speed or phase velocity in a medium. Calculating the index of refraction for a material provides insight to how dispersive it is and the potential for

it to be used in a spectrometer. The dispersive element in the spectrometer is only part of the entire instrument.

Dispersive spectrometers typically have an objective lens as one of the first components to collect light from a source, followed by elements that collimate the light prior to reaching the dispersive element. The dispersed light is then focused onto an imaging array by focusing lens. A slit limits the field of view of the system so that only one wavelength band falls onto a single row of pixels. Figure 3 is a basic example of a dispersive spectrometer. This research utilizes a prism as the dispersive element. Greater detail for how this dispersive spectrometer operates and how the instrument forms images on the focal plane array (FPA) are provided in Chapter 3 in the Instrument Description Section.

The second type of spectrometer, called an interferometer, measures interference to determine the frequency of emitted wavelengths. To create interference, a basic interferometer utilizes a beam splitter to equally divide incoming light into two separate paths, as shown in Figure 4. The light paths are then reflected back by two mirrors and recombined. One of the mirrors is moved to change the distance traveled by one of the light paths and therefore introduces a phase shift. As shown in Figure 5, this phase shift creates interference patterns consisting of constructive, bright regions, or destructive, dark regions, interference [21]. This pattern is called an interferogram. Computing the Fourier transform on the resulting signal reveals the spectrum of the

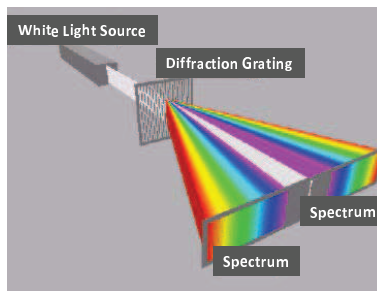


Figure 2. An example of a grating [9].

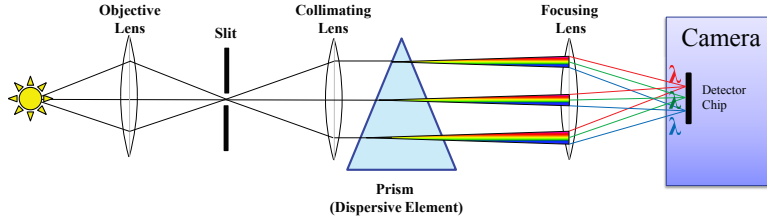


Figure 3. An example of a dispersive spectrometer.

light source [35].

To create an image of the scene, optics, such as an objective lens and a collimating lens, are placed in front of the entrance slit of an interferometer and a single diode detector is placed at the exit of the interferometer. After an interferogram is created for one portion of the scene, scanning mirrors are used to image another portion of the scene. Scanning continues in this manner until the entire scene is captured. To eliminate the need for scanning, some instruments use a focal plane array detector, but to date these instruments remain uncommon due to cost.

Both types of imaging spectrometers, dispersive spectrometers and interferometers, are called hyperspectral imagers if they collect data over many spectral bands, and both types have been placed on airborne platforms. Most airborne/space-based hyperspectral sensors can be categorized as spatial limited imagers or staring imagers

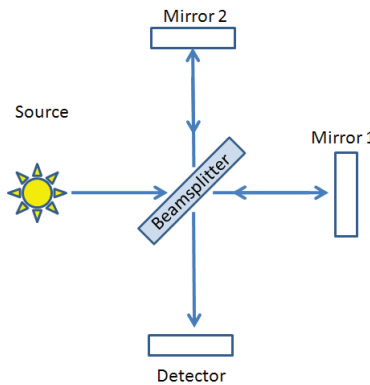


Figure 4. An example of an interferometer.

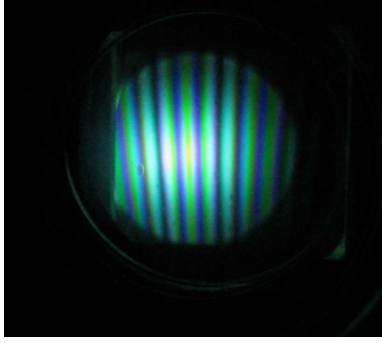


Figure 5. An example of an interference pattern created by an interferometer. The bright regions of the image is where constructive interference occurs. The dark regions of the image is where destructive interference occurs.

[15]. Spatial limited imagers capture a wide spectrum over a narrow spatial area, typically one dimension as the field of view (FOV). The single diode detector described in the previous paragraph is an example of a spatial limited imager. To capture the second or additional spatial data, the sensor must move or sweep. A push broom sensor, as illustrated in Figure 6, is an example of this type of sensor. The narrow FOV is the main disadvantage of spatial limited sensors.

Staring sensors collect two dimensional spatial data over a broad spatial scene by imaging an area for a relatively long period of time. During this time, the sensor is collecting spectral data in discrete bands over the spatial area. An imager utilizing a variable bandpass filter is an example of a staring sensor. The long stare time and the requirement for the scene to remain static are disadvantages for staring imagers. If part of the scene shifts during their collection time, then spatial and/or spectral

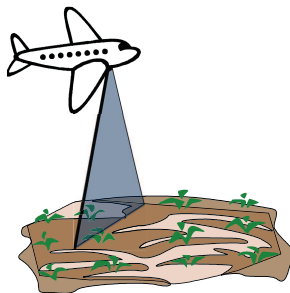


Figure 6. An example of a push broom hyperspectral sensor.

artifacts will exist in the collected data.

Staring sensors and spatial limited imagers typically have relatively long data acquisition times of 0.1 s to many seconds. CT imagers collect data by imaging the entire scene in each frame and can collect data at rates in the 10's of Hz, and potentially up to 100's of Hz. This is because CT imagers, do not stare or scan a scene, but instead captures the entire scene and all of the spectral data for that scene in a single frame. Greater detail is presented in the Data Acquisition Section in Chapter 4 of how a CT instrument collects spectral data in this manner. Because CT imagers can collect all of the incoming light for an entire scene with a single frame, they have decreased data acquisition time and increased signal strength when compared to staring or spatially limited hyperspectral imagers.

As an comparison of the increased signal strength, a CT imager could collect an entire n by n pixel scene on one frame. A hyperspectral imager with an entrance slit opening of a pixel wide by n pixel tall slit would be required to collect n frames to replicate the same scene the CT imager captured in a single frame. The overall signal strength for slit based hyperspectral imagers would be $1/n$ as much as a CT based system. This means the signal to noise ratio (SNR) for background limited detection of a CT based imager is $1/\sqrt{n}$. This increase in signal and the reduction of data acquisition time allows for the collection of data of rapidly evolving scenes.

Although airborne/space-based hyperspectral imaging has traditionally focused on static scenes or scenes with a limited FOV, the space-based system that AFIT is designing should be able to collect hyperspectral data from transient scenes. Previous research has proposed that chromotomographic imagers are capable of capturing and characterizing transient events such as bomb explosions, rocket launches, and lightning strikes over a broad spatial area [3; 18; 28]. Such a system may be able to provide insight into battlefield events such as identifying missile launches and chemical

compositions of explosions.

1.2 Current and Previous Chromotomographic Systems

To avoid confusion about what type of imager is being described, a brief listing of abbreviations and names utilized to describe these instruments is provided. Abbreviations such as “CTI”, “CTH”, “CTIS”, and “CTHIS” and names such as “chromo-tomographic”, “chromotomography”, “computed tomography”, and “computed tomographic” have been utilized throughout literature. For simplicity, this paper will utilize “chromotomographic imagers” and “CT” to describe all of these instruments. CT imagers are described in-depth in Chapter 2. For the purposes of this paper, CT imagers are divided into two main classes. Because the instrument described in this research utilizes a DVP as its dispersive element, all such instruments will be grouped together. All other CT instruments will be discussed in a separate group. To begin the description of CT imagers, the non-prism based CT instruments will be described first.

1.2.1 Non-Prism CT Systems.

Chromotomographic imagers, with the ability to capture temporally evolving scenes, have been around for more than a dozen years [14]. Descour, et al. were among the first to build a CT imager capable of capturing transient events outside of the laboratory environment. Their system utilized a two-dimensional computer-generated-hologram grating as the dispersive element and operated nominally in the visible range of the spectrum. The system acquired data during a missile launch, imaging at 30 frames per second (fps). Although not tested, the system had the capability to collect up to 60 fps. Compared to a reference spectrometer, the CT imager produced “spectra in good agreement with spectra taken by a reference non-imaging

spectrometer”. This was one of the first examples of the ability to capture rapidly evolving scenes that CT imagers possessed.

In 2006, Gat, et al. developed CT imagers utilizing fiber optics as the entrance slit to a spectrometer [17]. Because the scene is imaged first onto fiber optics, their instrument has the ability to capture a two dimensional image quickly as opposed to the limited FOV interferometers discussed in Section 1.1. Their instrument produced spectral results in agreement to a reference spectrometer of an evolving scene; however, their system has low spatial resolution due to the length of the input slit. The exact time scale on which their instruments operate is not known and overall documentation of their instruments is lacking. However, they have shown the ability to exploit the spectral information of two rapidly evolving scenes, one of a model rocket engine and the other of high voltage discharge in air.

1.2.2 Prism-based CT Systems.

In 1997, Mooney, et al. became the first group to build and demonstrate a CT imager utilizing a DVP as the dispersive element [26]. The imager they built operated nominally in the 3-5 micron band, the Mid-wavelength infrared region. The group also developed a reconstruction algorithm that was unlike those previously utilized in CT data reconstruction. The group tested their imager on a static scene in a laboratory setting. The main emphasis of their work was to test the an earlier theory of reconstructing CT collected data without the loss of any information [25]. A subsequent set of experiments were conducted against a static scene outside of the laboratory setting with a new instrument and an improved reconstruction algorithm [27]. The algorithm and reconstruction methods they developed has the claimed potential to reduce the volume of missing data from as high as 26% without data filtering (6.5% with filtered data) to 2%. The results from the experiments provided

spectral data that was similar to a scanned slit configured spectrometer that was used as a reference instrument; however no data was provided about the effectiveness in the reduction lost information during the reconstruction process.

Other subsequent CT imagers have been constructed and tested by Mooney [28; 33; 32]. However, each of the selected targets have been stationary scenes of cars, buildings, vegetation, and/or laboratory based experiments. Most of these results were compared with calibrated instruments. However, there is little information on the instrument’s performance with transient scenes.

Bostick has also developed a laboratory based CT imager utilizing a rotating DVP as the dispersive element [3]. The instrument operates in the visible region and was shown to have good spatial and spectral resolution against a laboratory based static scene. The characterization that he presents of his CT imager provides some of the most in-depth analysis of CT imagers currently available in literature [4]. Bostick has also written about systematic errors present in CT imagers [5].

In 2009, Wagadarikar, et al. became the most recent researchers to publish a new design of a CT imager [34]. Their instrument utilizes a coded aperture and a bandpass filter as part of the optical train. A non-rotating double Amici prism is the dispersive element in their design. As a proof of concept, the group imaged differing flame colors at 30 fps over an extended period of time. When compared to a reference spectrometer, the results suggest that their instrument was “able to correctly measure” spectra.

The above CT imagers have explored the possibility to capture and spectrally exploit transient events. The field deployable instrument built by AFIT is the fastest known rotating prism CT imager.

1.3 Organization of Thesis

This paper is divided into four additional chapters. Chapter 2 discusses the basics of prisms and how their dispersive properties are utilized in CT. Additionally, a brief discussion of the potential advantages of prism based systems is outlined. Chapter 3 begins with a discussion of the various components of the instrument and why they were selected. The chapter continues with an explanation of some considerations taken when data was collected with the instrument. Chapter 4 describes how the data was acquired for later processing, provides a brief background of current algorithms utilized to process CT captured data, and ends with a discussion of the reconstruction algorithm utilized in this research. Results and analyses are presented in Chapter 5. The chapter starts with an overview of the instrument and algorithm performance when collecting data on a static point in a high contrast environment. Next, results and analyses of an extended static broadband spectrum scene are presented. Chapter 5 ends with the spectral reconstruction of a transient scene. The final section of the paper discusses conclusions about the research and presents some recommendations for future studies.

II. Theory of Prism-Based Chromotomographic Imagers

The selection of a prism-based CT imager for this research is based upon many factors. As such this chapter will present background information of CT imaging. First a brief discussion of the historical link of CT imaging and the medical community's x-ray tomography is provided. Then a description of typical basic components utilized in CT instruments is provided. This is followed by a discussion of some advantages of prism-based CT imagers when compared to other CT instruments. The chapter concludes with an explanation of the dispersion of prisms.

2.1 Chromotomography's link to X-Ray Tomography

The "chromotomography" term was derived from the medical community's "x-ray tomography". Many of the reconstruction algorithms utilized in CT image processing are derived from the medical community's tomographic reconstruction algorithms. Chromotomography is similar to x-ray tomography in the fact that the goal of both imaging technique is the collection of a 3-D image. X-Ray tomography captures a 3-D spatial image by rotating two x-ray imagers around a stationary object. The x-ray imagers are placed 180° from each other and rotate concurrently around an object throughout a 360° collection. Unlike x-ray tomography, chromotomography produces a data cube, as previously described, that is composed of two spatial dimensions and one spectral dimension. The division of the spectral dimension into multiple bands, i.e. "colors", is where the "chromo" portion of the name was derived for these imaging instruments. To create the multiple bands of light, most CT instruments utilize similar components in their composition.

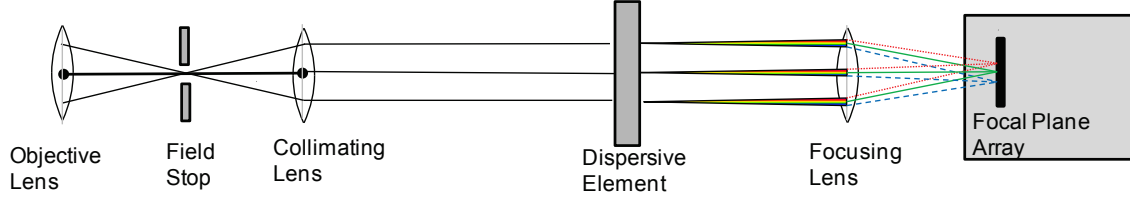


Figure 7. A typical layout of a CT instrument.

2.2 Typical Components of CT Imagers

CT instruments typically consist of an objective lens, field stop, collimating lens, dispersive element, focusing lens, and FPA, as illustrated in Figure 7. The objective lens focuses light from the target image to pass through the field stop. The field stop is required so that the entire dispersed image falls within the boundaries of the FPA. A further explanation of the importance of a field stop is provided in the algorithm portion of this document, Chapter 4. A collimating lens is utilized so that light enters the dispersive element as parallel plane waves (i.e. collimated light). If light entering the dispersive element is not collimated, then precise knowledge of wavelength dispersion will not be known. The dispersive element is the next optical element and as previously discussed is usually a prism or a grating. As the name suggests, the final lens focuses the dispersed collimated light onto the FPA. Without the final lens there would be no image on the FPA. The FPA then images the incoming spectrum for later data processing. AFIT's CT instrument was constructed with components similar to those in this paragraph. Based upon the advantages a prism has over a grating, a DVP was selected as the diffracting element in AFIT's instrument.

2.3 Advantages of Prism-based CT Imagers

The AFIT CT imager was built utilizing two prisms as the DVP. Mantravadi contends that a prism based CT imager may have better spatial and spectral resolution when compared to a similar grating based CT imager [24]. Additional advantages of a prism over other dispersive elements, according to Bostick, include simplicity of system design and integration with other instrument components, lower signal-to-noise constraints, and ability to perform high-speed, non-imaging spectroscopy utilizing the same data collected for data cube reconstruction [4]. The two prisms that comprise the DVP utilized in AFIT's CT imager were selected as the diffracting element due to their dispersion characteristics and are shown in 8.

2.4 Dispersion of Prisms

Dispersion of a prism can be predicted by calculating its index of refraction. Snell's law is commonly used to calculate the angle of refraction in prisms and other materials. Because the index of refraction is wavelength dependent, the refracted angle is also wavelength dependent. The angle is given by

$$\frac{\sin \theta_1}{\sin \theta_2} = \frac{v_1}{v_2} = \frac{n_2(\lambda)}{n_1(\lambda)} \quad (2)$$

$$n_1(\lambda) \sin \theta_1 = n_2(\lambda) \sin \theta_2, \quad (3)$$

where θ_1 is the angle relative to the surface normal of the incident light; and θ_2 is the angle relative to the surface normal that the refracted light propagates through material two. The index of refraction for material one and material two is denoted by n_1 and n_2 respectively.

The angle, δ , between the deviated light path that exits the prism and the path

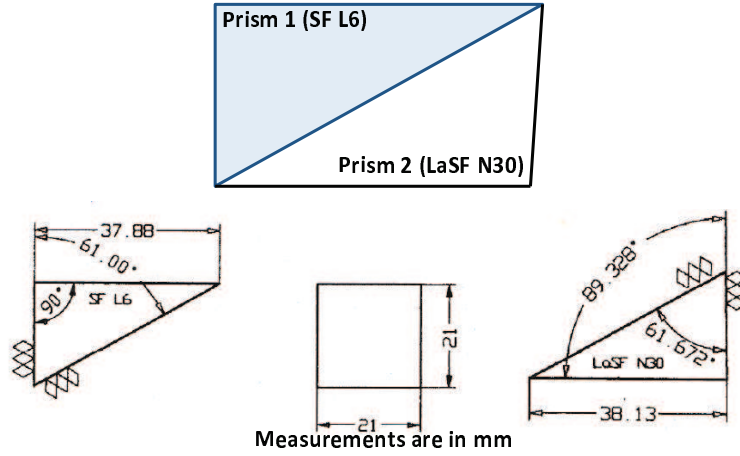


Figure 8. Drawing of the prisms utilized in the CT imager.

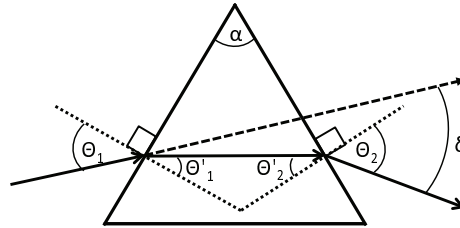


Figure 9. A graphical representation of dispersion in a prism.

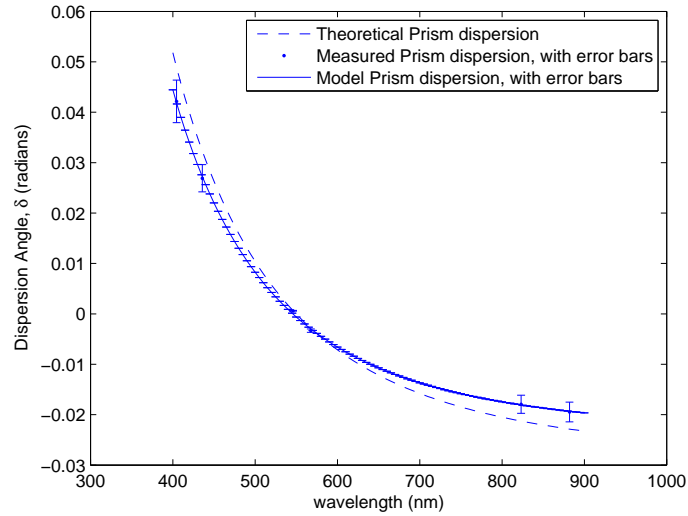


Figure 10. The graph displays the theoretical dispersion in prism a with a dashed line. The points, with vertical error bars, are the measured dispersion of Hg and Xe pen lamp sources. The solid line, with horizontal error bars, is the power equation utilized to model the actual dispersion of the prism.

the ray of light would have taken if no deviation would have occurred is given by

$$\delta = (\theta_1 - \theta'_1) + (\theta_2 - \theta'_2), \quad (4)$$

where the angles are defined as shown in Figure 9. The angle between the surface normals and the path of light through the prism is represented by θ'_1 and θ'_2 . The angle of light entering and exiting the prism relative to the surface normals are respectively represented by θ_1 and θ_2 .

The theoretical and actual dispersion of the prisms were calculated and measured and are displayed in Figure 10. The actual dispersion of the prisms closely follows the expected results and is further discussed in Chapter 4. Knowledge of the actual dispersion of the prisms is required to properly reconstruct the data the CT instrument acquires. Once the actual dispersion was measured, a mathematical model could be created, see Equation 5, which is described in Chapter 4, and other components of the instrument could be selected. These components along with the experimental procedures utilized in this research are the next items discussed in this paper.

III. Instrument Description and Experimental Procedures

This chapter provides details of the components and insight as to how they were selected in the construction of AFIT's CT instrument. Experimental procedures, also discussed in this chapter, were then developed for the instrument.

3.1 Instrument Description

AFIT's CT imager has the same design as shown in Figure 7. A photograph of the instrument is displayed in Figure 11. Additionally, a top-view sketch of the instrument is displayed in Figure 12. A Vixen model R200SS, 8" Newtonian telescope serves as the objective lens. The telescope, an $f/4$, was selected as the objective lens based upon several reasons. These reasons include a pre-constructed sturdy structured system, an aberration free lens system (when compared to glass), and, more importantly, the focal point of the telescope was outside the body of the telescope. The location of the focal point of the telescope provided easy access to place the field stop. Attached to the telescope, in a tube assembly, is a turning mirror, an aperture, and a collimating lens. A tube assembly was used because of its rigidity and its ability to reduce the amount of ambient light reaching the FPA. If further light reduction was required for the instrument, an optical blanket was placed over the components not housed in the tube assembly. The turning mirror redirects the light from the telescope through the rest of the optical train. A turning mirror was added to minimize the width of the instrument so the instrument could fit on a single tripod. An adjustable aperture placed at the focal point of the telescope serves as the field stop to ensure the camera's detector is not overfilled. The next optical element is an achromatic lens.

Achromatic lenses are utilized for the collimating and focusing lens to reduce aberrations of the imaged scene. An Edmunds 88.9 mm focal length lens with a 25.4



Figure 11. A picture of the field deployable CT hyperspectral imager on a tripod.

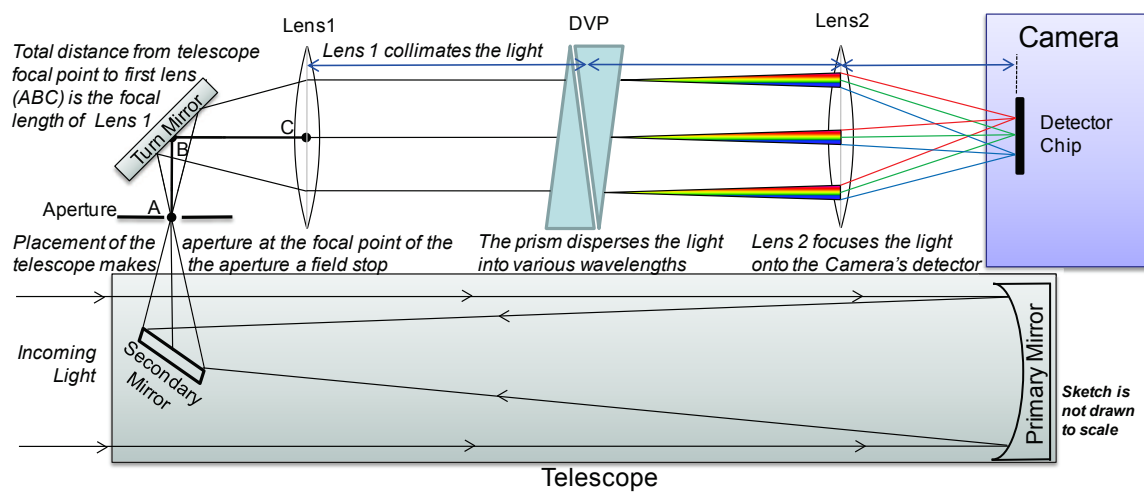


Figure 12. Sketch of the field deployable chromotomographic hyperspectral imager.

mm diameter was selected as the collimating lens. The diameter of the lenses were chosen based upon the DVP dimensions. Following the collimating lens was the DVP mounted on a rotation stage.

As stated earlier, two prisms function as the dispersive element. Two prisms are used so that one wavelength, approximately 548 nm, passes through the system un-deviated while all other wavelengths are deviated at various angles. The prisms are joined together by optical contact and are made of Schott LaSF N30 and SF L6 glass 8. For non-point sources, the dispersion of the scene results in the stacking, or overlap, of spectral images on the FPA. Spectral images are images of the scene in narrow wavelength bands. To separate the spatial and spectral data of each frame, numerous frames of the same scene need to be taken at numerous prism rotational angles. The overlap of spectral/spatial data and the separation process of the data is further explained in the next chapter. To obtain the differing prism angles, a rotation stage rotates the prisms along a fixed axis.

The rotation stage was a CM-5000 series motor/encoder built by Allied Motion Technologies Corporation. A custom made housing encased the rotation stage. The CM-5000 was selected because it could nominally operate at 25 Hz and could provide angular position data which is instrumental in data reconstruction.

A side note about the rotation stage must be mentioned at this point. Due to a manufacturer's error, operating the encoder with the manufacturer's suggested controller card could never be accomplished and therefore the motor/encoder never reached full potential. Instead, a power supply with a variable voltage setting was utilized to operate the motor at angular rates less than 25 Hz and without angular position location data. A new motor/encoder has been bought for future use in the instrument. Consequences of not utilizing an encoder that could provide precise prism rotation angles are detailed later in this document.

The next optical element following the DVP is a focusing lens; an achromatic Thor Labs 75 mm focal length lens with a 25.4 mm diameter is the focusing lens. The lens is fixed in place in a tube assembly attached to the camera. Counterintuitive to the naming scheme, only the collimating lens was adjusted for focusing this instrument on a scene at the various scene distances used. By adjusting only the collimating lens, the linear dispersion should theoretically remain constant throughout the differing ranges of the experiments. The focusing lens focuses the image onto a camera's FPA.

A black and white Vision Research Phantom v5.1 camera is utilized as the FPA and records the images. The Phantom v5.1 camera operates nominally in the 400-900nm wavelength region and has a spectral response that matches well with the dispersion curve of the direct vision prism 10. The spectral response, shown in Figure 13, of the camera was measured utilizing a white light source and a monochromator. The camera has a silicon based complementary metal oxide semiconductor (CMOS) detector as the FPA. The Phantom v5.1 has the ability to capture up to 1,200 fps at the full resolution of 1024 x 1024 pixels. Table 1 displays some of the maximum recording rates for the various image sizes. Other framing rates and resolution options not listed in the table are possible. A laptop, with Vision Research supplied software, was used to control the camera and store the data. The Phantom software is capable of storing images or movies in various formats such as "mpeg" and "avi." The avi format was utilized for easy import into MATLAB. Additionally, LabVIEW software installed on the laptop controlled the rotation stage through a data card and power supply.

All of the optical components, except for the telescope, were securely attached onto an optical bread board. Optical alignment of the camera was accomplished by utilizing a standard lab jack to control the vertical adjustment and a translation stage to control the horizontal alignment. The breadboard was then placed within an

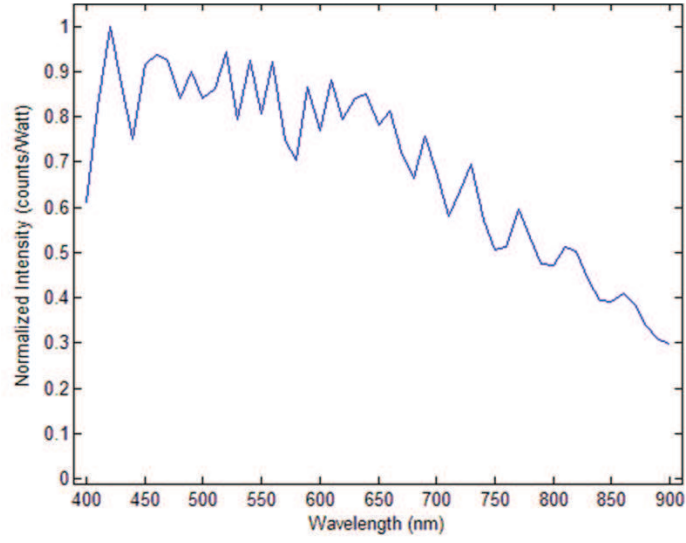


Figure 13. Spectral Response measured by utilizing a white light source and a monochromator for Phantom v5.1 Camera.

Table 1. Phantom v5.1 maximum fps. Data courtesy of Vision Research [30]

Resolution(pixels)	Rate(fps)
1024x1024	1,200
768x768	2,140
512x512	4,380
256x256	13,400
128x128	33,900
64x64	66,300
64x32	95,000

aluminum structure that also held the telescope. In this configuration, an aluminum “cage” held the telescope in place. All elements of the instrument could be adjusted horizontally and vertically except for the rotation stage. The aluminium structure was designed by and structurally modeled by a group of astronautical engineering students at AFIT [2]. They tested various structural integrity components such as bending and vibration. The aluminum structure was then placed on a tripod to ease deployability when conducting field tests. After the instrument was constructed, various experiments were conducted to characterize the imager.

3.2 Experimental Procedures

Because of the simplistic nature of the algorithm used in data reconstruction, scenes with high spectral and spatial contrast were chosen to facilitate confirmation of the spectral results the algorithm provided. An American flag, because of the distinct stripes, is an example of a scene with high spatial contrast. Pen lamps, such as a mercury pen lamp, that have strong emission lines located 10’s of nm apart is an example of a scene with high spectral contrast. Prior to the collection of any data, the focusing lens was focused and then permanently set in position. Ideally the lens would have been set at precisely one focal length away from the FPA, thereby setting its focus on an object at infinity. An alternative method utilized to set the position was to focus the lens at an object far away simulating infinity. To set the focal length of the focusing lens, the lens was attached to the Phantom camera via tube assembly and was then focused on a tower’s obstruction light located approximately six miles away. This was the furthest object that could be imaged with high contrast. To ensure that collimated light was collected for a given scene at a given range, the collimating lens was adjusted until a reference point source in the scene occupied the fewest number of pixels on the camera’s detector. This was done without the prism in

the optical train. Otherwise, a clear focus was difficult to achieve during the focusing on a scene.

For many of the scenes, ambient light sources were kept at a minimum. This was done in an effort to achieve the highest spectral contrast possible. To do so, some of the scenes were imaged at night while minimizing extraneous light sources, such as street lights. Additionally the exposure time of the camera was typically held very low. For example, the exposure time was typically around $900\mu\text{s}$ for the collection of pen lamp data in a dark room, and for a well lit daytime scene the typical exposure time was around $250\mu\text{s}$. Holding the exposure time to a minimum was done so the camera's CMOS detector would not become saturated, thus allowing spectral features to be more prominent.

During deployment of the instrument from one scene to another, parts of the instrument, such as the camera mount and parts of tube assembly, could move slightly and thus cause misalignments. The movement of the camera was due to the lab jack and translation stage used to mount it. The tube assembly housing the collimated lens could move vertically on one end as it was not securely fastened to another part of the instrument. These components were not fixed into place to allow adjustment. To offset any possible misalignments, a pen lamp would typically be imaged next to a target of interest. The pen lamp acted as a calibration source to verify the dispersion. To obtain the best results, ambient light of the scene was reduced by placing the pen lamp in a closed box that had a narrow opening cut in it. To make the pen lamp a point source, an aperture was placed in front of the pen lamp. In some instances, a laser pointer of a known wavelength and multiple pen lamps were used prior to scene collection. These procedures were a key component in the data acquisition process and enabled analysis of the data the simplistic reconstruction algorithm produced.

IV. Data Acquisition and Algorithm Development

To best understand the results that are presented in the next chapter, a comprehension of how data is acquired and how it is reconstructed is required. Therefore this chapter will begin with a discussion of how the data is acquired based upon instrument configuration. A brief synopsis of CT reconstruction algorithms is presented next, followed by algorithm selection and implementation.

Although algorithm development is not the main focus of the thesis, an understanding of how a reconstruction algorithm operates provides useful insights to the instrument and into CT imaging. Therefore a simple algorithm was developed to reconstruct the collected data. The simplistic nature of the algorithm had some impact in the manner of how data was collected for the research. Regardless of which algorithm is utilized to reconstruct data, some instrument considerations must be accounted for during data acquisition in order to achieve successful results.

4.1 Data Acquisition

As noted previously, a direct vision prism is the dispersive element used in the CT instrument. Two prisms are used so that one wavelength passes through the system un-deviated while all other wavelengths are deviated at various angles. In this manner, light from a polychromatic point source such as a Hg pen lamp (see Figure 14) would disperse similar to that shown in Figure 15. A pen lamp with an aperture, approximately a millimeter in diameter, placed in front of it was used to create the Hg pen lamp point-like source. Figure 14 is a Hg pen lamp as imaged through the instrument without the prism in place. When the aperture was illuminated by the Hg pen lamp, multiple images of the aperture were observed. Each image corresponds to the wavelength of a different emission line for the lamp. Figure 15 is dispersion of the

Hg pen lamp when the prism is in place. Because the Hg pen lamp is a stationary point-like source with few spectral features, the emission lines are easily discernable. However, when the scene has additional spectral and/or spatial elements involved, it is necessary to capture additional images of the scene at various prism angles in order to reconstruct the data spatially and spectrally.

Figure 16 provides a simplistic illustration of the stacking, or mixing, of spectral images on the FPA for a single frame. Once again a Hg pen lamp is the illumination source; however, this time it is being used to back illuminate a resolution chart as shown in Figure 17. To better understand what is occurring, a notional dispersion of a back illuminated resolution chart was created, Figure 18. Each emission line was color coded for ease of visualization. Four frames of differing prism rotations are projected onto the image. To capture differing prism angles, the prism is rotated along a fixed axis while the camera is capturing images. Coaddition of these images, which is explained in the “Algorithm Development and Description” portion of this chapter, can then be used to reconstruct the scene. Before discussion of the reconstruction algorithm, the temporal requirements of the system and the FOV requirements are explained.

In order to reconstruct a quickly evolving scene, the prism will need to rotate rapidly so that multiple prism angles can be imaged. For the best data acquisition, the prism should rotate at a rate so that no scene changes occur, i.e. the scene appears to be static in one prism revolution. Otherwise, the resulting data will have spatial and spectral artifacts in the reconstruction. To create a spectrally robust image, the camera will need to have a framing rate on the order of a hundred times the prism rotation speed. The high framing rate is required so that images of the scene at multiple prism angles can be captured and analyzed. The framing rate may be reduced if the scene has high contrast.

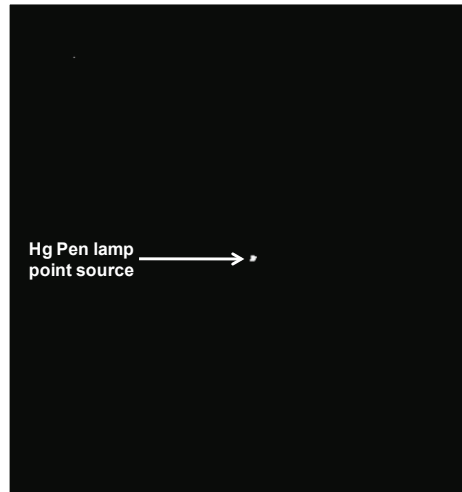


Figure 14. Picture of Hg pen lamp point-like source without the prism in the optical train

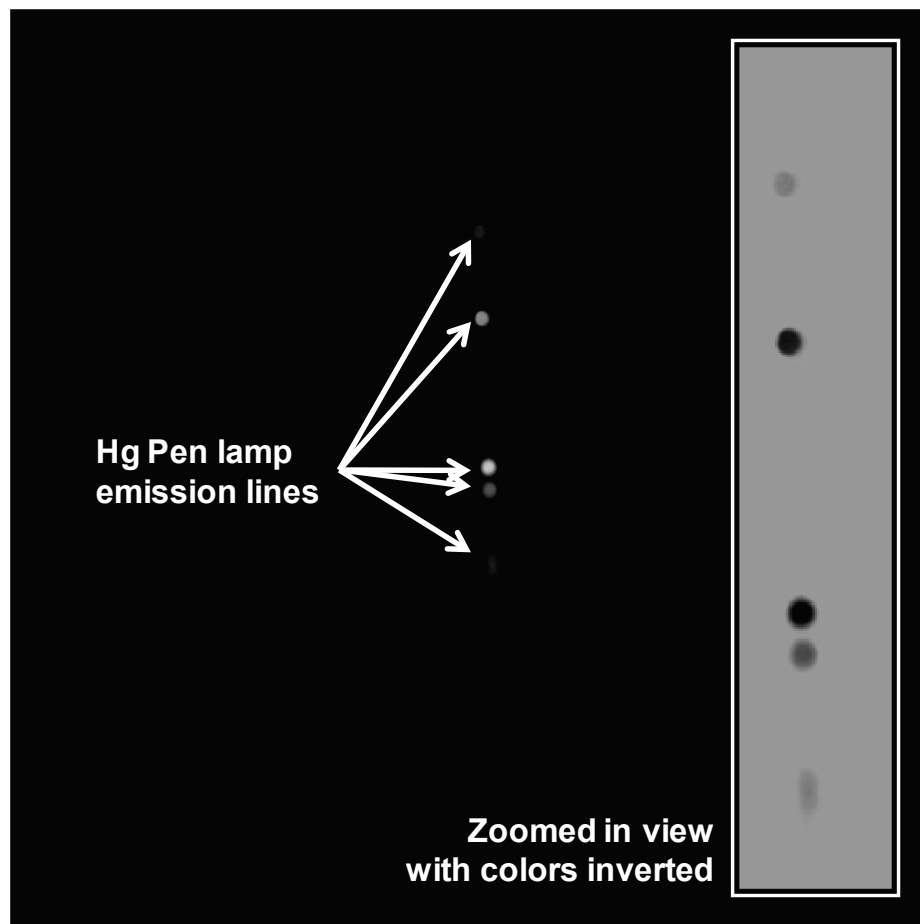


Figure 15. The dispersion of a Hg pen lamp point-like source seen when the prism is in place.

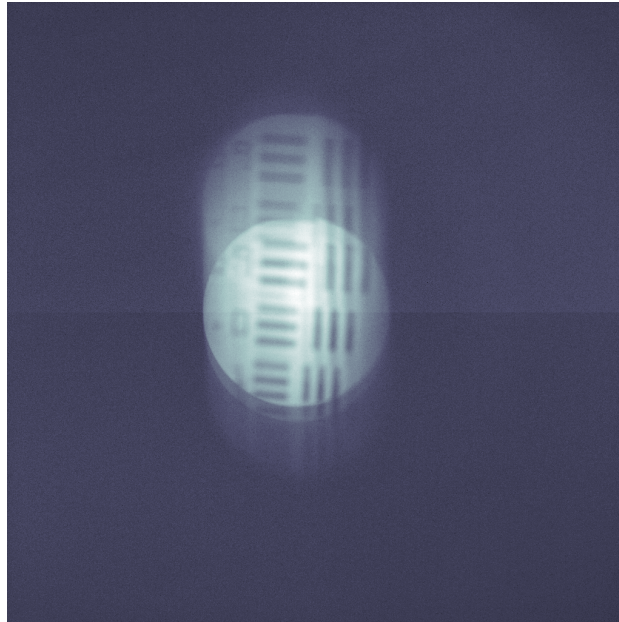


Figure 16. An image of a resolution chart illuminated by Hg pen lamp. Each image corresponds to an emission line. The contrast of the image was adjusted in post-processing so the differing images of the resolution chart could be more easily seen.

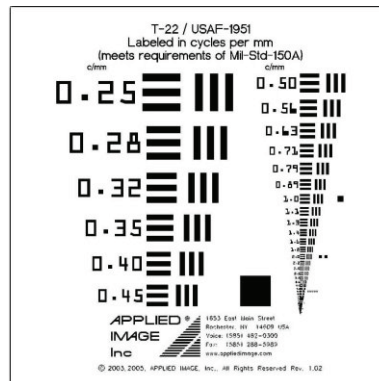


Figure 17. The T-22 USAF resolution chart, courtesy of Applied Images Inc., Rochester, NY.

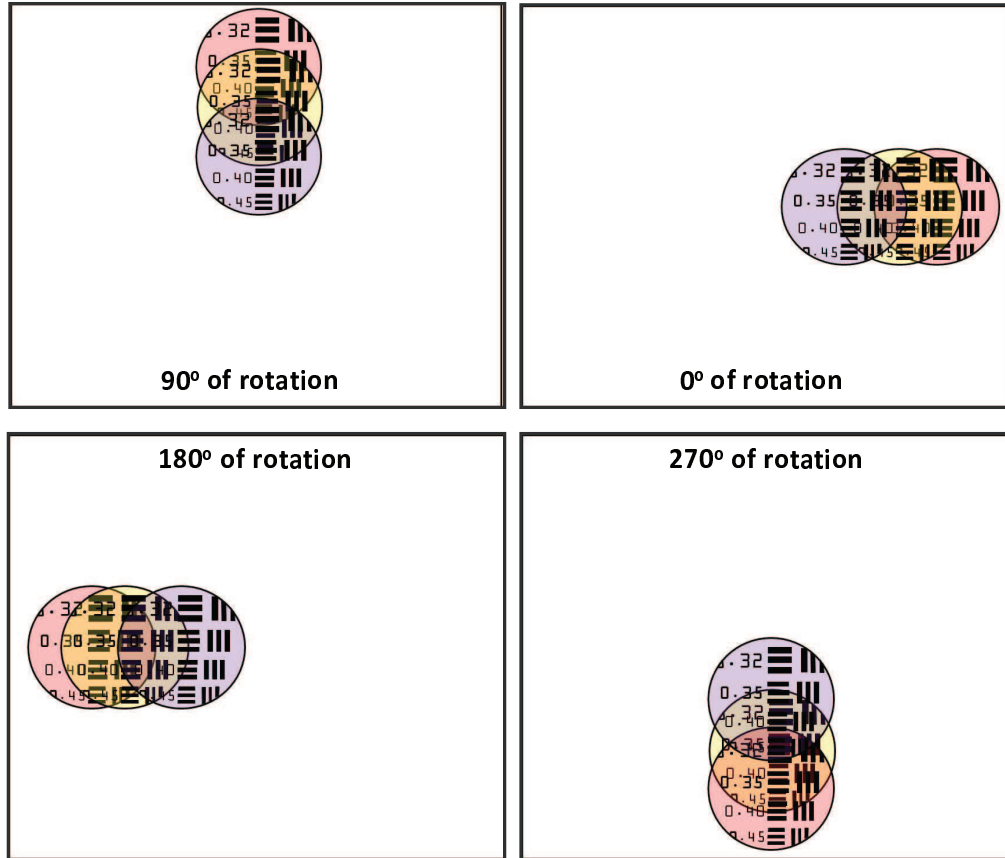


Figure 18. Notional dispersion of a back illuminated resolution chart. The notional source produces three emission lines, which are color coded for ease of visualization. Four frames of differing prism rotations are projected onto the image.

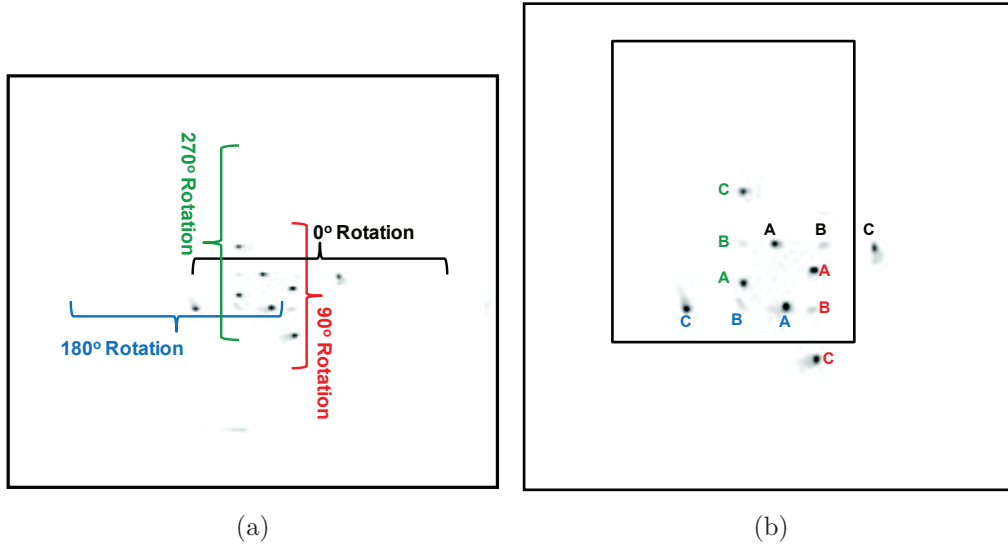


Figure 19. The above images were formed by summing multiple frames a Hg pen lamp at different prism rotation angles. (a) is four locations of prism rotation with full pixel resolution. (b) is a zoomed in version of the left image, where the boxed area represents a notional FOV. The different color of letters represents different angles and the different letters represent different emission lines. Because all of the scene does not fall on the notional FOV the FPA is overfilled.

An example of an evolving scene is a bomb blast. A bomb blast evolves at tens to hundredths of a second [29]. If an event evolved at a hundredth of a second, then the prism should complete one rotation at least as fast, a hundredth of a second, and the camera should frame at a hundred times the speed of the prism rotation rate, or 0.1 milliseconds. To capture these frames in such a transient event, or for that matter all data collection for this instrument, the Phantom camera ideally records a movie for at least one complete prism revolution.

The field of view is another important factor. If during scene acquisition part of the dispersion falls off of the Phantom camera's CMOS detector, then the spectral and spatial reconstruction resolution would be degraded. The Figure 19a shows a composite image of four prism angles for the Hg pen lamp. Figure 19b shows a boxed region representing a reduced FOV that is not centered about the point of prism rotation. To ease in visualization of the movement of the scene as the prism

rotates, each emission line has a corresponding letter next it and each prism angle is color coded. Because all of the scene does not fall on the notional FOV, the FPA is “overfilled”. If the only data available for reconstruction was contained in the boxed region, then spectral and spatial data from the scene would be incomplete and the reconstruction would not have as good of resolution as possible. Although, in this simple illustration the point sources could probably be reconstructed, the intensity of the resulting image would be reduced and might therefore lead to improper analysis of the data. Additionally, the reconstruction of a more spatially and spectrally diverse scene would either be degraded or not possible. A brief discussion of some other algorithms is next followed by an explanation of the creation of the reconstruction algorithm utilized in the research.

4.2 Reconstruction Algorithm

Many algorithms have been developed for various CT instruments. Algorithms are typically developed to improve the accuracy/completeness of the reconstruction while reducing computing time. The implementation and modification of an existing algorithm for a CT imager can be a research project by itself. For this reason, a simple algorithm was used in this research. However, a review of other algorithms is useful in understanding CT imagers.

4.2.1 Algorithm Background.

The earliest CT algorithms were built from existing medical tomographic imaging algorithms. A good overview of CT in the medical community is provided by Brooks and Chiro [7]. Because of the central slice theorem, performing a 2-D Fourier Transform of a 3-D object results in loss of data. Some of the earliest instruments and reconstruction algorithms resulted in a missing cone of data [13; 14]. Subsequently

a new CT instrument was constructed with the aim to reduce the amount of missing data through the use of a rotating prism and redundant captured spectral data [25; 27; 26]. In an effort to reduce reconstruction computing time and to compensate for the missing data, numerous reconstruction algorithms have subsequently been developed for rotating prism instruments [1; 6; 28; 12]. Previous AFIT research sought to improve the capability of algorithms utilized in reconstruction of CT instrument data [19; 20]. A good summary of many of these techniques and a good overview of CT in general can be found in a Sandia report written by Ford, Salazar, and Wilson [16].

However, as stated earlier, the implementation of these algorithms was not part of this research. An algorithm was created based upon a backprojection technique that has been utilized by another CT instrument built at AFIT [3]. Backprojection has been utilized by the medical tomography field for years and has been scrutinized against other reconstruction algorithms [11; 10]. Although backprojection will not always produce the best results when compared to other algorithms, it was one of the earliest reconstruction methods utilized, has well understood error, and is one of the simplest methods to implement[7]. Backprojection is a simple algebraic method that permits data to be reconstructed as it is collected and can be designed with increased complexity utilizing *a priori* knowledge of the scene [3]. For these reasons, backprojection was the selected method used in developing the reconstruction algorithm.

4.2.2 Algorithm Description.

A key part of the image processing algorithm was to find where an image with a given wavelength was located on the CMOS detector. Theoretically, one wavelength should pass through the direct vision prism, and therefore CT imager, un-deviated.

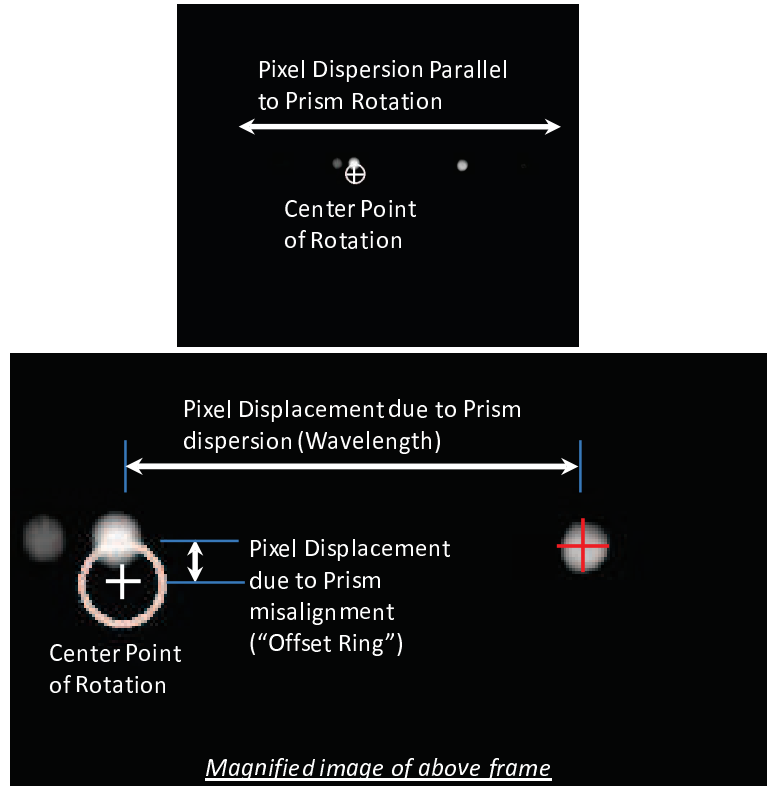


Figure 20. The top image is an example of the prism dispersion and the transverse shift associated with the central point of rotation. The lower image is a magnified version of the top image. Here the transverse shift of the prism along with the pixel shift due to prism dispersion is highlighted.

Furthermore, all other wavelengths would be dispersed along an axis corresponding to the prism rotation angle. During experimental validation it was discovered that there was an additional shift transverse to the dispersion axis; e.g. if a wavelength was expected to shift 90 pixels vertically, the actual result was a 90 pixel shift vertically and 20 pixel shift horizontally (the transverse shift). This shift is illustrated in Figure 20. The transverse shift of the dispersed wavelengths is due to the misalignment of the two prisms when they were put together.

If it were not for the transverse shift, the “un-deviated” wavelength through the prism and imaged on the FPA would appear to be stationary throughout a prism rotation. However the “un-deviated” wavelength’s path for a full prism rotation was actually a circle about some point on the FPA, as shown in Figure 21. The transverse shift of the dispersed wavelengths was found by summing multiple frames of a movie taken of a Hg pen lamp. The bright central circle shows the path the un-deviated wavelength took. This circular region was called the “offset ring.” The first step in data reconstruction was to correct for the offset ring model as well as inputs which detailed the prism orientation. Figure 22 displays a plot of the offset ring when a point-like source rotated about a pixel located at row 513 and column 555. For most of the recorded data, the shape of the offset ring was circular. However, sometimes the shape was slightly elliptical having axes of 44 and 48 pixels. The change in shape of the offset ring was typically small, four pixels at the most, and may have stemmed from camera movement that occurred during transportation between data acquisitions. Knowing the size and location of the offset ring allowed for the wavelength specific displacement along the dispersion axis to be determined.

To determine the wavelength specific displacement, six points from Hg and Xe pen lamps were utilized to develop the wavelength and pixel deviation equation. Figure 23, a composite image of three pen lamps, shows the dispersion of Hg, Xe, and Ne

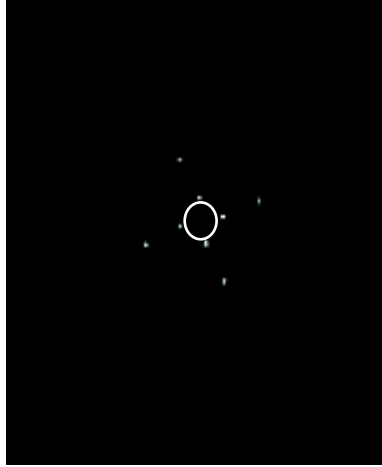


Figure 21. Image formed by summing multiple frames of a movie of an Hg pen lamp. The bright central circle shows the path the un-deviated wavelength took. This circular region was called the “offset ring.”

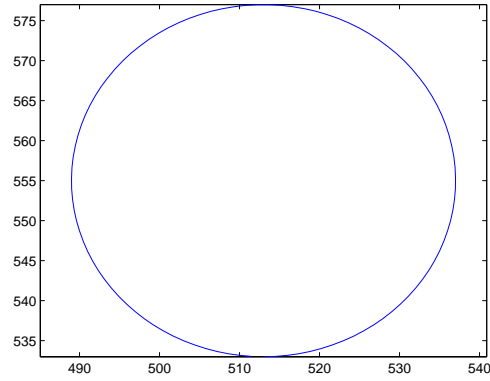


Figure 22. Plot of “offset ring” pixel locations used in the reconstruction algorithm.

Table 2. Observed spectral lines with deviation from un-dispersed wavelength.

Element	Wavelength (nm)	Deviated (pixels)
Hg	405.65	-275
Hg	435.83	-175.5
Hg	546.08	-4
Hg	567.71	21.75
Xe	823.16	117
Xe	881.94	127

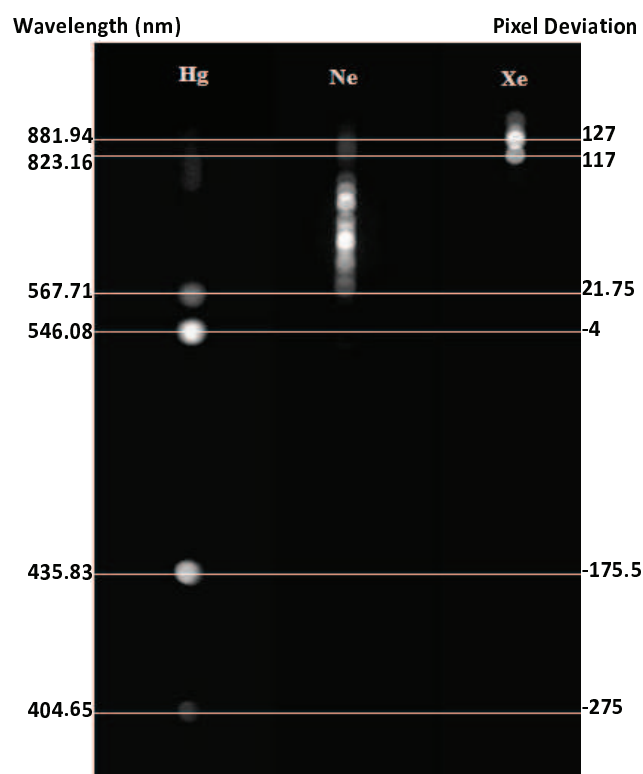


Figure 23. A composite image of different pen lamps.

pen lamps. Table 2 displays the six points from Hg and Xe pen lamps utilized in the wavelength and pixel deviation equation. The emission lines for the Ne pen lamp were too closely spaced to easily discern and were not used to derive a wavelength and pixel deviation equation. To calculate the pixel deviation, the centroid displacement for each of the six points, Figure 23, was measured from the center of the offset ring. Wavelength numbering for each of the six points was derived from pen lamp manufacturer and National Institute of Standards and Technology (NIST) data.

Since the dispersion for the prism is very low for long wavelengths and high for short wavelengths, see Figure 10, the data was fit to a power model. The model used had the following format

$$f(x) = a * x^b + c. \quad (5)$$

Where a , b , and c are coefficients used to fit the curve, x is wavelength, and $f(x)$ is the pixel deviation. MATLAB's curve fitting tool was used to find a fit of the data. The coefficients and the confidence are listed below in Table 3. Using the calculated coefficients, it is possible to implement an algorithm in MATLAB to reconstruction scene data at known wavelengths.

Because the prism rotates during data acquisition, angular position of the dispersed data is also required to reconstruct the data. For illustrative purposes, 104 frames of movie data of a notional wavelength during prism rotation was created. Figure 24b displays row and column positions for the offset ring for this data. Figure 24b is the nominal wavelength, 708 nm, which equates to a dispersal location of 92

Table 3. Best fit parameters for the model.

Coefficients	Coefficient values	(95% confidence bounds)
a	-2.474e+011	(-7.478e+011, 2.531e+011)
b	-3.36	(-3.7, -3.019)
c	157.4	(141.9, 173)

pixels. These figures illustrate how the data for a particular wavelength rotates on the FPA during data acquisition. Path knowledge of the dispersed data and knowledge of the size of the scene on the FPA can be utilized to select a narrower FOV for image reconstruction. As an example, the target wavelength for reconstruction of a dispersed scene may be limited to 301×301 pixel² region on a FPA with a full resolution of 1024×1024 pixel². The “shift and add” algorithm utilized to reconstruct data requires the offset ring’s size and location to be known.

To recreate data for a given frame from a captured scene, the algorithm creates a new image of the narrowed FOV centered on the target wavelength’s column and row position. For one prism revolution, the algorithm continues to create new images for each of the frames captured. These frames are then added together to reconstruct the scene at a particular wavelength. An illustrative example of the shift and add algorithm is provided next.

Figure 25 is a notional shift and add reconstruction of a resolution chart of Figure 18. The target wavelength is shown in the bottom left hand corner of the Figure 25. The four circles of differing prism rotation angles represent the wavelength and FOV that was utilized in the reconstruction. In each prism rotation angle, the spectral and spatial data from the other emission lines are partially projected onto the FOV for the wavelength of interest. This partial projection of other emission lines is a function of the prism dispersion. The addition of the four frames produces the reconstructed image shown at the right of Figure 25 . Utilizing the shift and add algorithm, the reconstruction of a weak emission line and/or a reconstruction that had a limited number of prism angles, and therefore frames, produces a picture with relatively strong spectral and spatial artifacts from the other emission lines. The reconstruction of a stronger emission line and/or more frames of differing prism angles produces an image that has relatively weak artifacts and possess better spatial and spectral

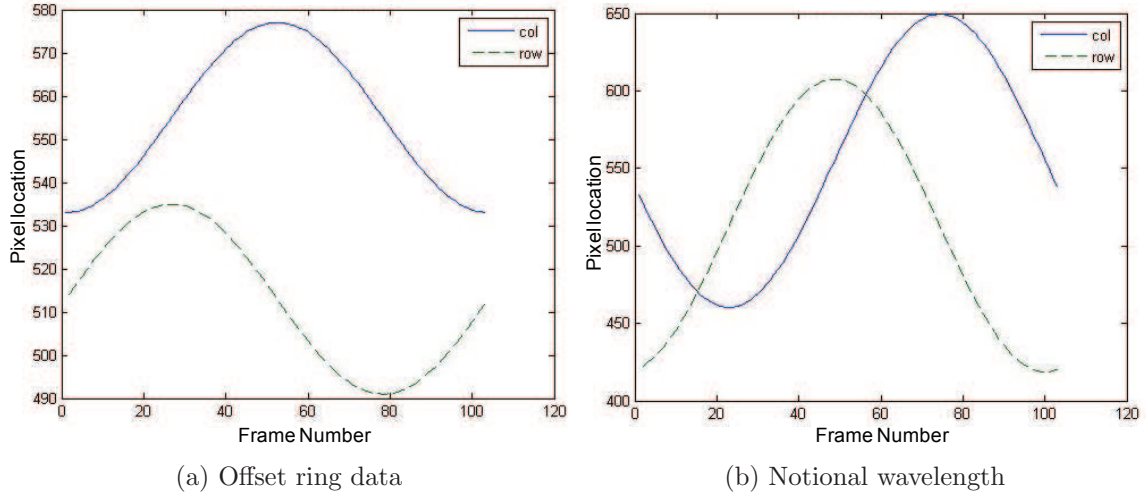


Figure 24. (a) is the column and row locations for where the “offset ring” was located in during the 104 frames. (b) is the location for a wavelength, 708 nm, having a displacement of 92 pixels.

resolution. Actual reconstructions of a resolution chart back illuminated by a Hg pen lamp is presented later in this section, see Figure 28 .

For data reconstruction, the algorithm was mostly implemented by shifting dispersion location by a certain number of pixels. Because the prism dispersion is not linear, see Figure 10, the reconstructed data created by pixel shifts will not be in uniformly incremented wavelengths, as is the case for many of the figures in Chapter 5. Alternatively, utilizing the power model equation 5 described above, a shifting of dispersion location by wavelengths was implemented when the desired reconstruction was for a particular spectral feature. This method, also seen in figures in Chapter 5, was utilized when recreating pen lamp data. Additionally, a loop was created in the algorithm for the purposes of automating data cube creation.

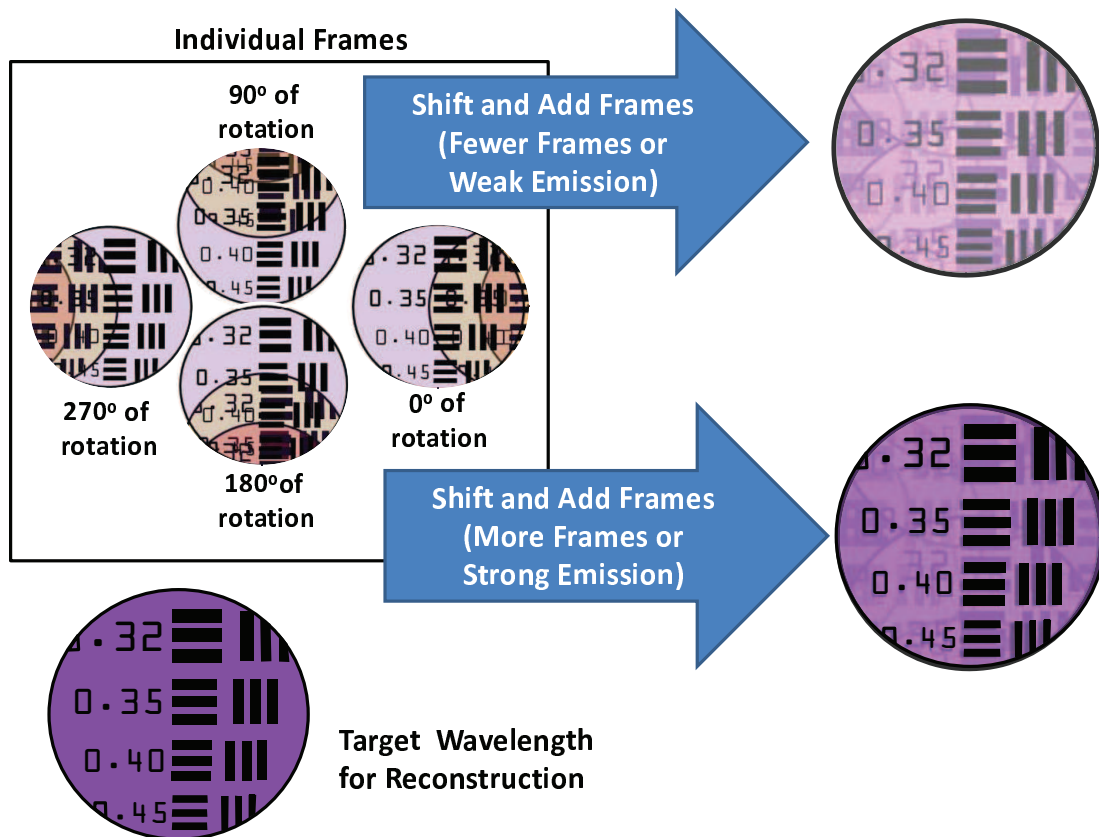


Figure 25. This is a notional “shift and add” reconstruction of a resolution chart, that is back illuminated by a source that produces three emission lines 18. The target wavelength is shown in the bottom left hand corner of the figure. The four circles represent that wavelength and FOV for four frames of differing prism rotations. Note how spectral and spatial data from the other emission lines are projected onto the FOV for the wavelength of interest. The addition of the four frames produces the reconstructed image on the right portion of the figure.



Figure 26. A reconstructed wavelength image of a point-like source that is “on-wavelength.” Because the reconstructed image is similar to a point source, an emitted spectral line is at that wavelength.

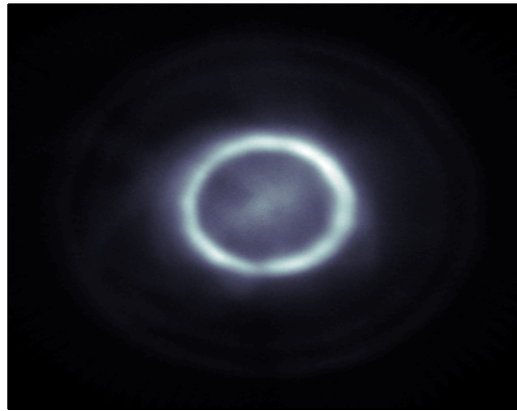


Figure 27. A reconstructed image of a point-like source that is “off-wavelength.” Because the reconstructed image is a ring and does not resemble a point source that was imaged, there is not an emitted spectral line at the reconstructed wavelength.

One example of data cube creation is the use of the algorithm to reconstruct a scene by intervals of a ten pixel shift. Due to the camera’s spectral response (see Figure 13) the data was processed within the visible to the very near infrared region of the spectrum, nominally 400 nm to 850 nm. This data cube for a 301×301 pixel² reconstructed FOV would consist of 21 spectral bins of data.

One method to verify that the reconstruction algorithm works properly is to reconstruct a point source. An expected result of an emission line reconstruction for a point source would result in a point reconstruction, such as displayed in Figure 26. This reconstruction of an emission line is termed “on-wavelength.” Reconstruction of a wavelength outside of an emission line is termed “off-wavelength.” An expected result for an off-wavelength reconstruction would be a ring or multiple rings, such as displayed in Figure 27. Rings will sometimes be present in an on-wavelength reconstruction of points sources and are an artifact of the simple shift and add algorithm. Rings are present because no noise filtering, i.e. removal of off-wavelength images, was implemented in the data reconstruction.

For a spatially diverse scene, such as the resolution chart back illuminated by a Hg pen lamp, an on-wavelength reconstruction would result in an image with higher intensity as shown in Figure 28 or a low intensity image as in Figure 29 for an off-wavelength reconstruction. To verify if a point-like source was properly reconstructed, a plot of the intensity for the central row region of the reconstructed FOV could be made. Using the reconstruction mentioned in the previous paragraph, Figure 30 consisting of nine bins was created. The bins where the intensity is a peak is where an on-wavelength reconstruction occurred. This algorithm did not employ any filtering for noise resulting from off-wavelength artifacts. Therefore, the spectral and spatial resolution of the reconstruction will be limited, especially for diverse scenes. Utilizing this simplistic algorithm, various scenes ranging from static with high spatial

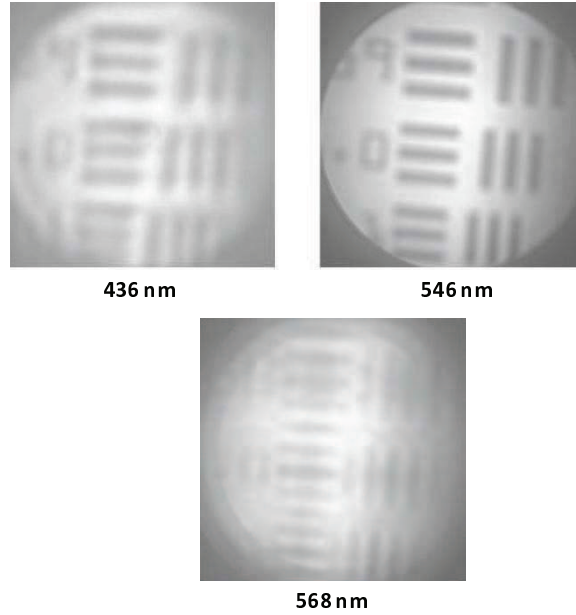


Figure 28. Processed images of resolution chart illuminated by a Hg lamp, see Figure 16 at emission lines located at 436, 546, and 568 nm. The image at 568 nm is blurred due to the small signal and proximity to the more intense image at 546 nm.

and spectral contrast, to transient events were recorded in avi file format. The file was then imported into MATLAB where reconstruction was executed by the shift and add algorithm as previously described. These scenes and their reconstruction outcomes are discussed in the next chapter.



Figure 29. Image at 650 nm. As expected, there are no discernable features since there is not a Hg emission line at this wavelength.

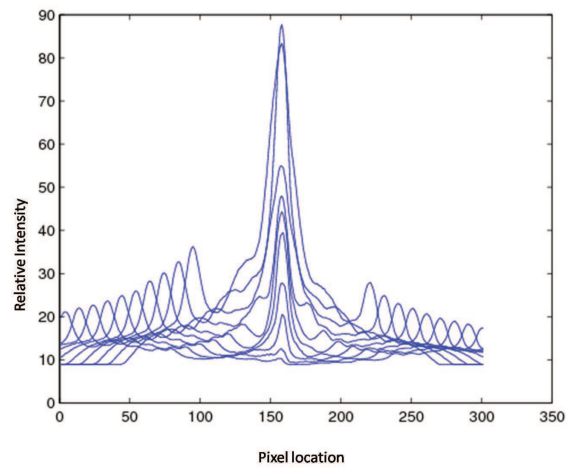


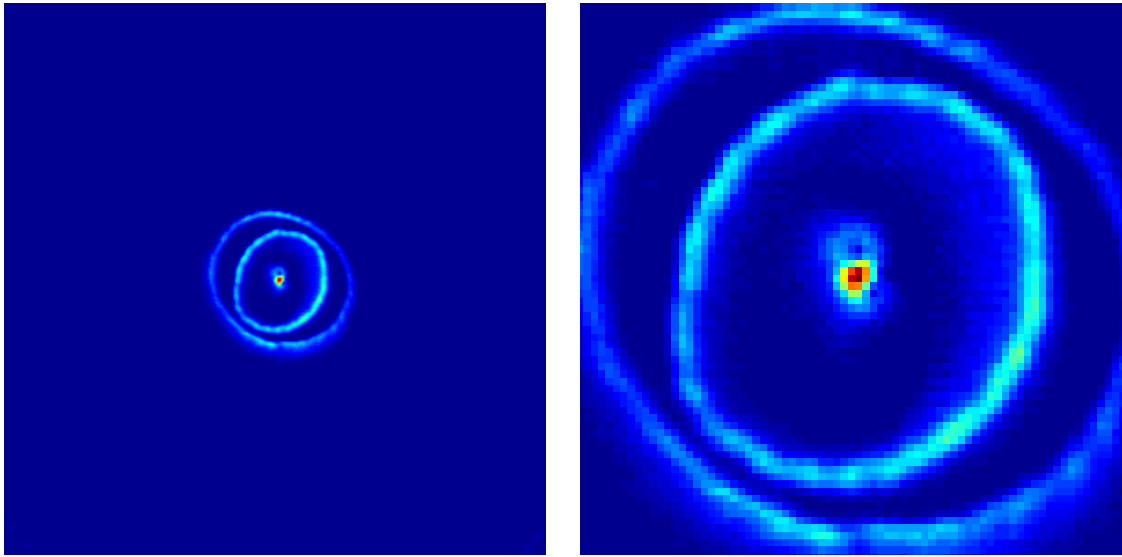
Figure 30. A plot of the intensity of nine reconstructed bins for a point-like source. The bins where the intensity is a peak is where an on-wavelength reconstruction occurred.

V. Experimental Results and Analysis

The CT imager was tested on a variety of outdoor scenes at differing ranges illuminated with different natural lighting conditions. To characterize the system and accuracy of the algorithm, an initial set of measurements were collected at night with targets with high spectral contrast. Collection of targets then progressed to a static, broad spectral scene with high spatial contrast; imaging of an American flag during the day. Finally, the instrument was used to collect transient events (fireworks) with low light conditions. Except where noted, each reconstruction utilized an avi file of one prism rotation. Most of the images presented below were created using the algorithm discussed in Chapter 4. In order to better visualize the images, each image is displayed utilizing the “imagesc” display option in MATLAB. This function automatically rescales the image by dividing the entire frame by the peak intensity level for the image and then multiplying by a coefficient. The rescaling created images of the reconstructed scene that were more visibly discernable.

5.1 Algorithm and Instrument Performance

The algorithm performance and the instrument calibration were first validated in data collection with a Hg pen lamp and a laser pointer in the scene. The experiment occurred outdoors at night with a distance of approximately 100 m from the target to the instrument. An aperture was placed in front of the pen lamp in order to achieve a point-like source. The laser pointer was illuminating the front of the aperture near the opening. The initial reconstruction of 568 nm for the Hg pen light, as illustrated in Figure 31, assumed that the system was in perfect alignment and that the motor rate was constant. The reconstructed image is not a perfect point-like source located in the middle of the frame as expected. Instead, the reconstructed image has a point-



(a)

(b)

Figure 31. The reconstructed intensity image of a point-like source located at 568 nm assuming constant rotation rate. Image (a) is a 301x301 pixel² reconstruction. Image (b) is a zoomed in version of the reconstruction.

like source with a “halo” located above it. This reconstruction error is likely due to motor mount misalignment as described by Bostick [5]. Additionally, as can be seen in Figure 31, the reconstruction resulted in artifacts that were not circular as expected. This is possibly due to an imbalance in the motor resulting in an inconsistent rotation rate or is possibly an additional result stemming from motor mount misalignment.

To overcome the motor mount misalignment and motor imbalance, the position of the centroid for the point-like source was found at each frame. This data was then used as the location for dispersed point-like source rather than assuming a constant dispersion vector based upon prism angle. The shift and add algorithm, discussed in Chapter 4, assumes a constant dispersion vector. The centroid position vector was then utilized to reconstruct the image shown in Figure 32. In this reconstruction, the image recreates a point-like source as expected. Figure 33 displays the two reconstructed images utilizing the “precise” dispersion location at the centroid of the point-like source and the “estimated” constant dispersion vector location of the point-like source. A logarithmic scaling was applied to the reconstruction utilizing centroid location to highlight how the artifacts are now concentric circles as opposed to ellipses.

A plot of the row and column positions of the two reconstruction methods is shown in Figure 34. The plots appear to be very similar in nature with only a few pixels difference for a given row or column position. The difference in position between the two reconstruction methods is shown in Figure 35. The plot on top illustrates the column and row difference and the plot on bottom illustrates the actual vector difference between the two reconstruction methods. For most frames the error is limited to only a couple of pixels; however, there are frames where the vector difference is as high as four pixels.

Figure 36 illustrates the intensity and the line width of the four central rows

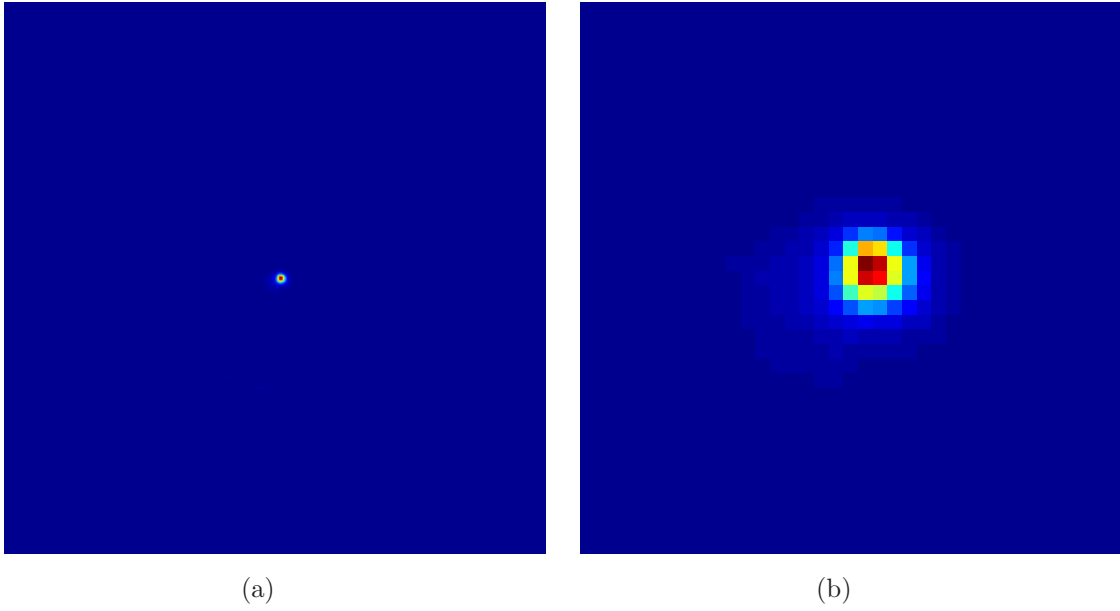


Figure 32. The reconstructed intensity image of a point-like source located at 568 nm utilizing precise centroid position. Image (a) is a 301x301 pixel² reconstruction. Image (b) is a zoomed in version of the reconstruction.

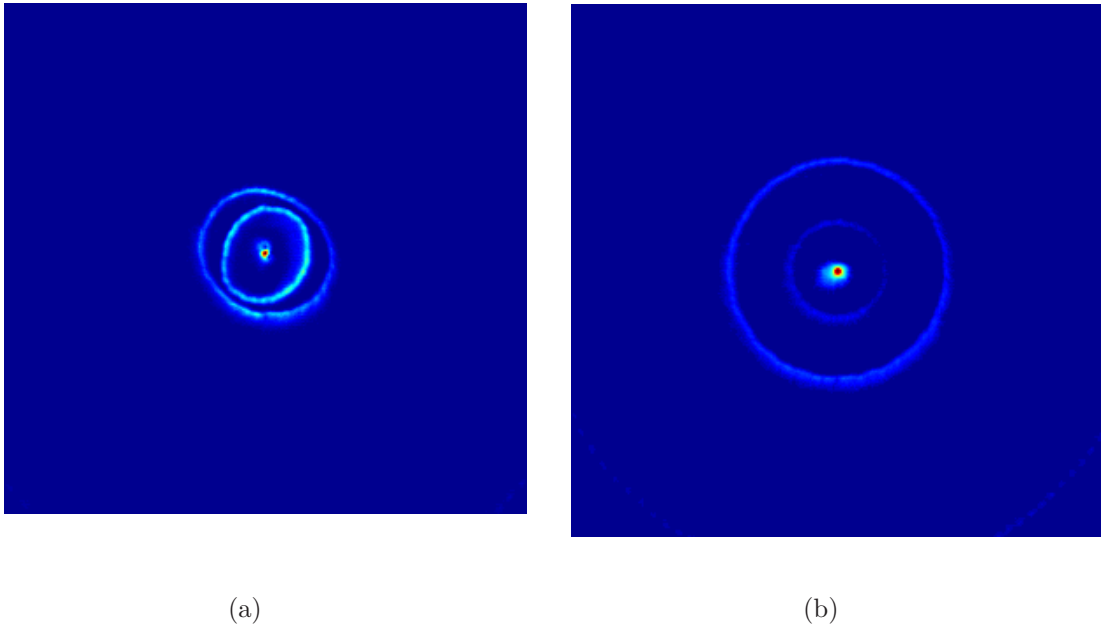


Figure 33. Image (a) is the reconstructed intensity image of a point-like source assuming constant rotation position. Image (a) is the same image as in Figure 31a. Image (b) is a scaled reconstructed intensity image of a point-like source utilizing precise centroid position. The image was created by taking the logarithm of the original intensity and then utilizing “imagesc” to display the result.

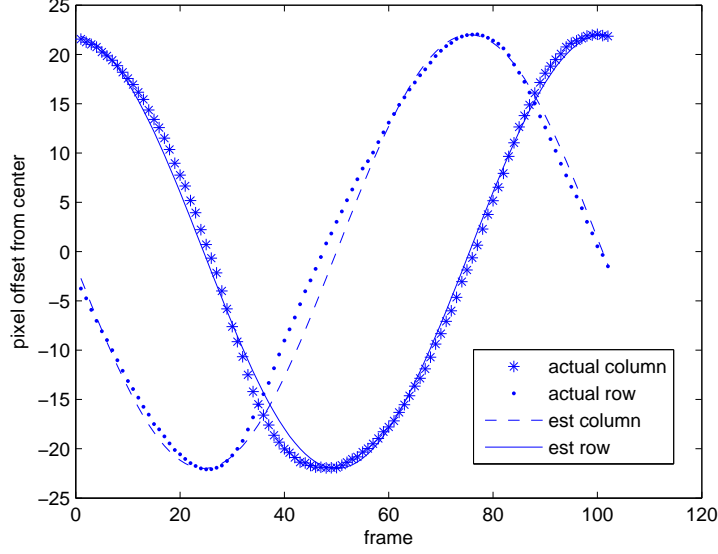
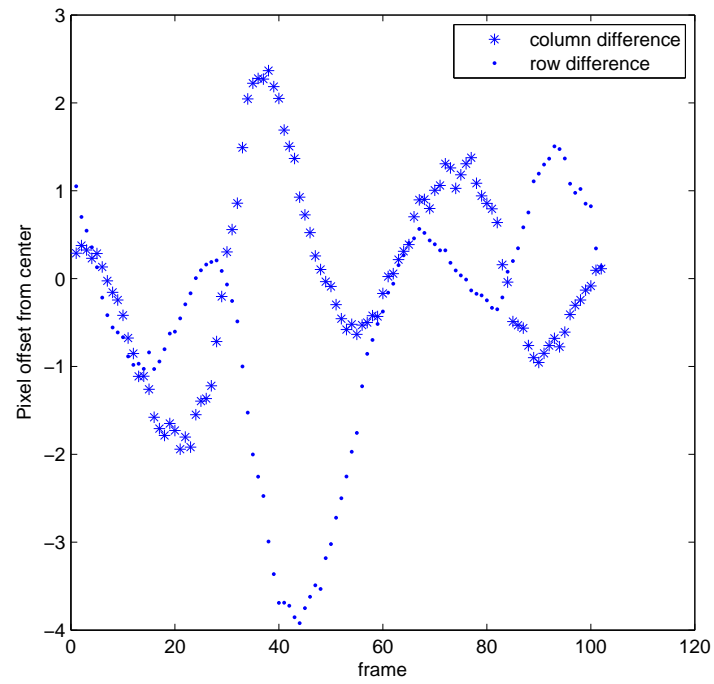


Figure 34. A plot of the row and column positions of the actual center of a point-like source compared to the estimated center.

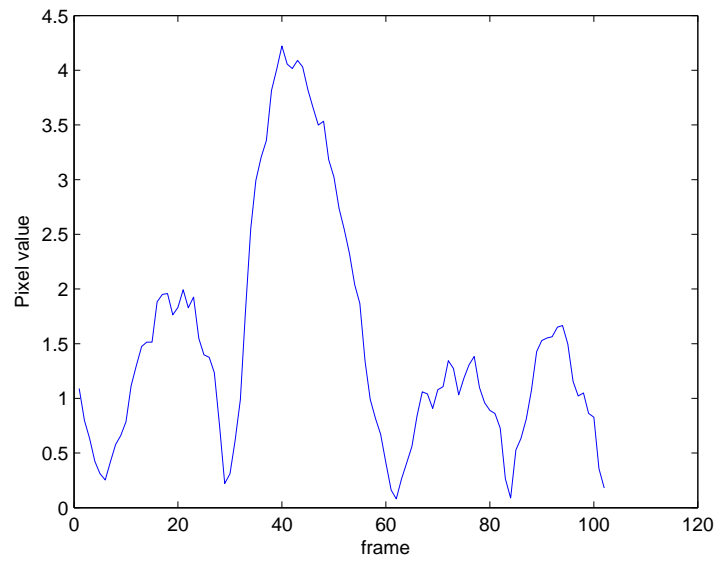
summed together in the y-axis of each reconstruction methods. The relative intensity is approximately 15 times higher for the reconstruction utilizing the centroid location and the full width half max for each reconstruction are approximately the same. The increase in intensity for the “estimated” reconstruction near the edges of the plot is due to the artifacts of the reconstruction, i.e. the off-wavelength spectral lines of the Hg pen lamp.

Even though the “precise” reconstruction provides the best results, the overall effectiveness of the “estimated” algorithm is adequate enough to reconstruct the collected data for the subsequent tests documented below. These test and the reconstructed data illustrate the abilities the instrument possess to capture varying scenes.

The need to use the centroid location of a point-like source illustrates that the CT imager is somehow misaligned and/or improperly balanced. System alignment is essential for space-based and fixed systems. Many steps have been taken to achieve the best alignment possible for this instrument. Prior to field tests the instrument was calibrated in a laboratory setting, where optical alignment could be accomplished

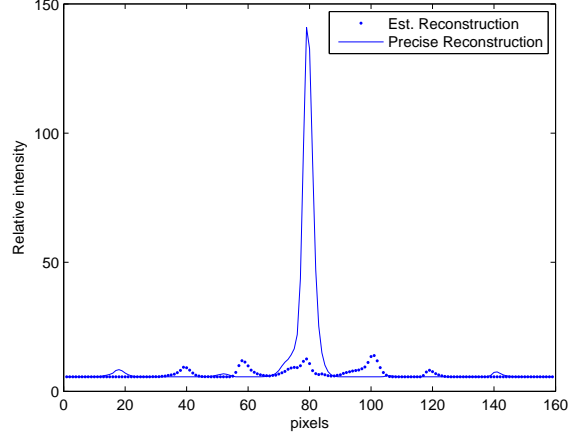


(a)

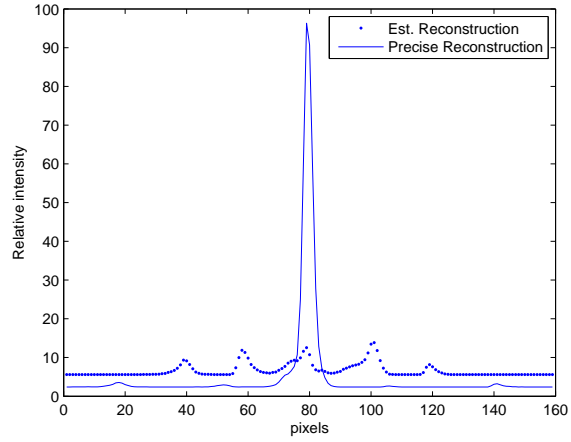


(b)

Figure 35. Plot (a) is the difference between the centroid location of a point-like source compared to the estimated center location. Plot (b) is the vector difference between the two locations.



(a)



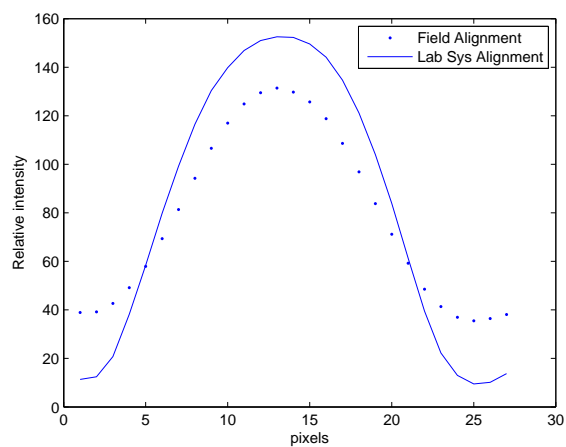
(b)

Figure 36. A plot of the intensity line width comparison of the “precise” and “estimated” reconstructed images. Plot (a) is most of the reconstructed frame. Plot (b) is the same FOV as in (a); however the the precise plot intensity was divided by the minimum value to highlight the off-wavelength artifacts. Off-wavelength artifacts are the smaller peaks located outside of the main peak in the center. The center peak is 568 nm, the peaks located at 60 and 100 pixels are 546 nm and the peaks located at 40 and 120 pixels are 436 nm emission lines.

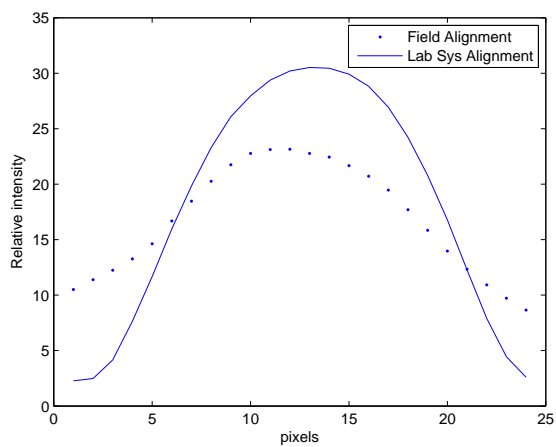
in great detail. However, movement of the instrument to the field over uneven terrain caused misalignment. Re-calibration of the instrument occurred in the field after movement and prior to data acquisition. However, the field alignment was time consuming and was not as precise as the laboratory calibration. A comparison reconstruction spot size of a point source for the two calibration methods can be seen in Figure 37. Although the peaks of the two calibration methods appear similar in shape, the original spot size of the point-like source in the laboratory alignment was approximately 22 pixels in diameter while the spot size for the field alignment was approximately 7 pixels in diameter. Even though the field alignment method broadened the reconstructed scene, it was adequate for the purposes of the research.

Before proceeding to the other results achieved during the Hg pen lamp test, two other points when utilizing the “estimate” reconstruction should be noted. First, as discussed in Chapter 3, the precise starting and ending angle of the prism is not exactly known as no encoder was utilized. Second, the center of rotation/dispersion is also not exactly known for most scenes. For a point source, such as the Hg pen lamp, these locations are relatively easily found; however, for a scene without a calibration source, these locations are estimated. This estimation could result in dispersion and wavelength assignment inaccuracies. Given the available equipment, these inaccuracies have been minimized as much as possible.

The “estimated” shift and add reconstruction was utilized for the rest of the Hg pen lamp/laser pointer data and for most of the results in this paper. Figure 38 shows the results of this utilizing this algorithm to reconstruct the laser pointer (635 nm) and the Hg emission lines of 436 nm and 546 nm were then reconstructed. Each image returns a scene which resembles a point-like source. The 546 nm reconstruction presented the best results due to the imagesc scaling reducing the off-wavelength artifacts and the relative strength of the emission line. The 436 nm and the 635 nm



(a) 546 nm plot



(b) 568 nm plot

Figure 37. Plots in (a) are the relative reconstructed spot size of the laboratory alignment and the field alignment for 546 nm. Plots in (b) are the relative reconstructed spot size of the laboratory alignment and the field alignment for 568 nm.

reconstructions display the errors previously discussed.

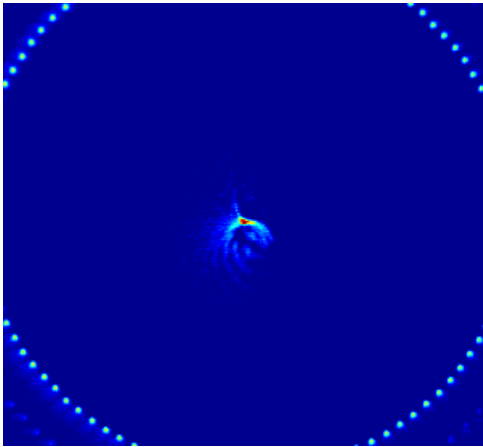
The results here show that the system is capable of acquiring higher fidelity data if the alignment could be improved. However, the estimated reconstruction will be sufficient to explore the ability of the system to capture transient events. For completeness, a hypercube is presented in Figure 39. The reconstruction begins at 440nm and increases in 10nm increments up to 550nm. Point like reconstructions can be seen in 440nm and 550nm due to the proximity to Hg emission lines of 436nm and 546nm.

One note about the camera can be highlighted with these reconstructions. When the camera was in operation for long periods of time, the bottom half of the CMOS array would image at higher intensities than the top portion as seen from the semicircle artifact in the 420 nm, 430 nm, and 440 nm reconstructions a semicircle artifact is in the lower half of each frame.

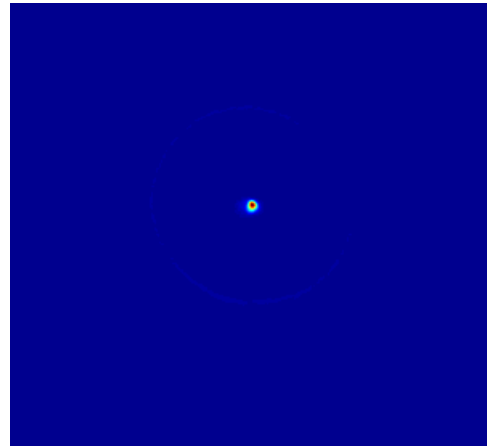
5.2 An Extended Scene, Broadband Spectrum

To test the ability of the imager to record an extended scene with a broadband spectrum, an American flag illuminated by the sun was imaged at a distance of 100 m during midday. The flag was chosen as a source due to its high spatial contrast of the stripes and the blue field. The flag was stationary during the imaging. The unprocessed image of the flag as captured by the instrument and a reconstructed image are shown in Figure 40. The reconstructed image was created by the addition of hypercube data collected from approximately wavelengths 500 nm to 700 nm. Images outside of this range were not as visibly clear as those within this range. A possible reason for this can be explained by looking at individual pixels of the flag.

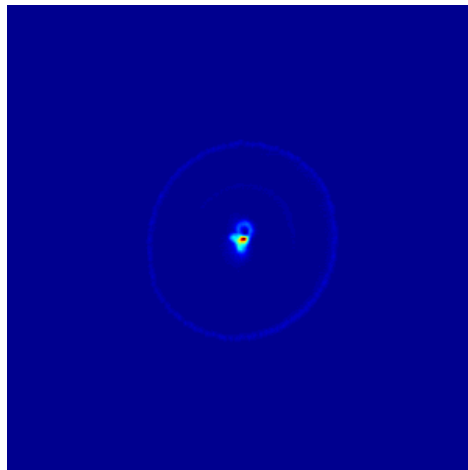
Figure 41 shows the locations of the individual pixels that were selected for further exploration and also the spectra of those pixels. The intensity plots were created



(a) 436 nm



(b) 546 nm



(c) 635 nm

Figure 38. Reconstructed intensity images of a point-like source at 436 nm, 546 nm, and 635nm.

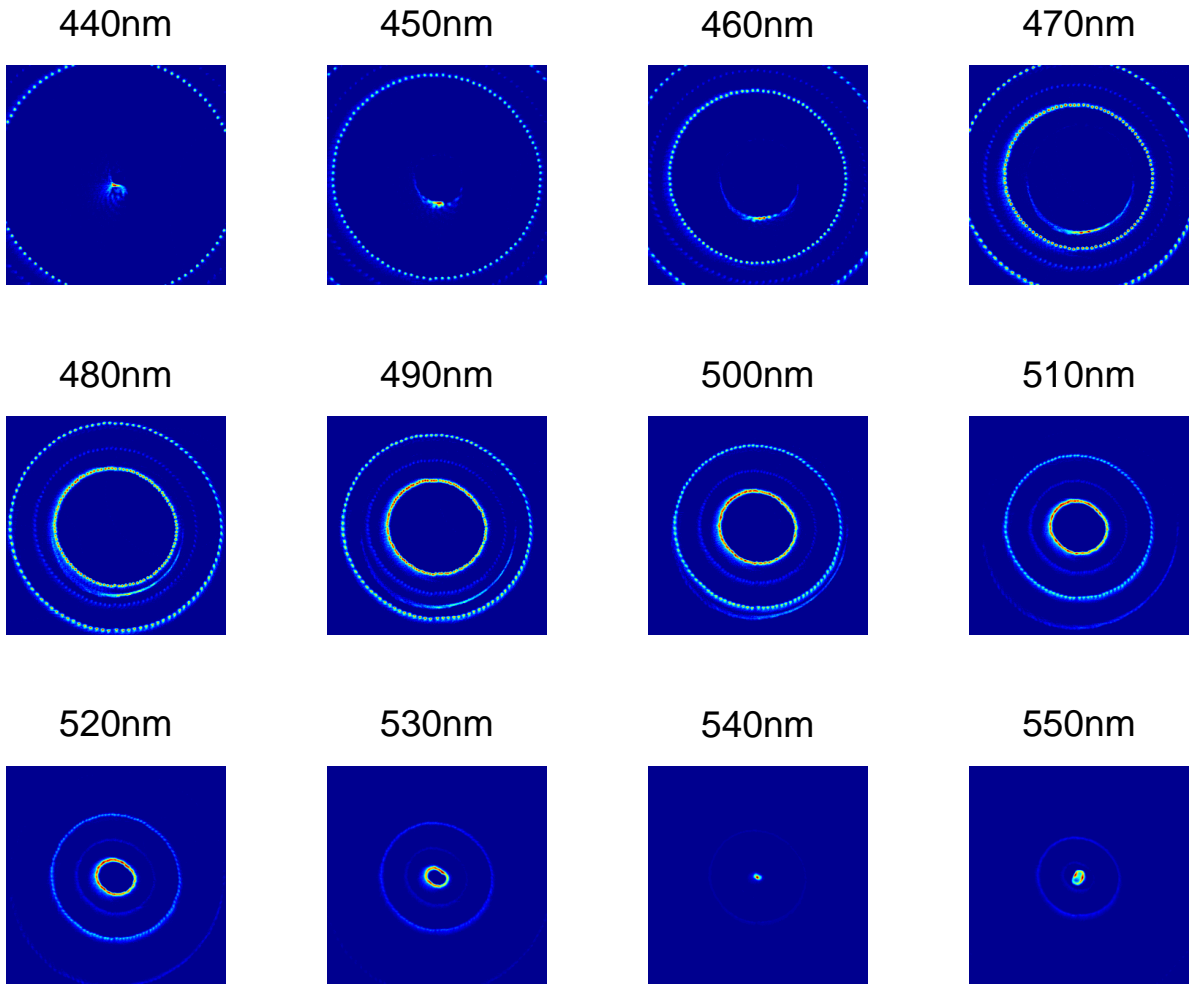
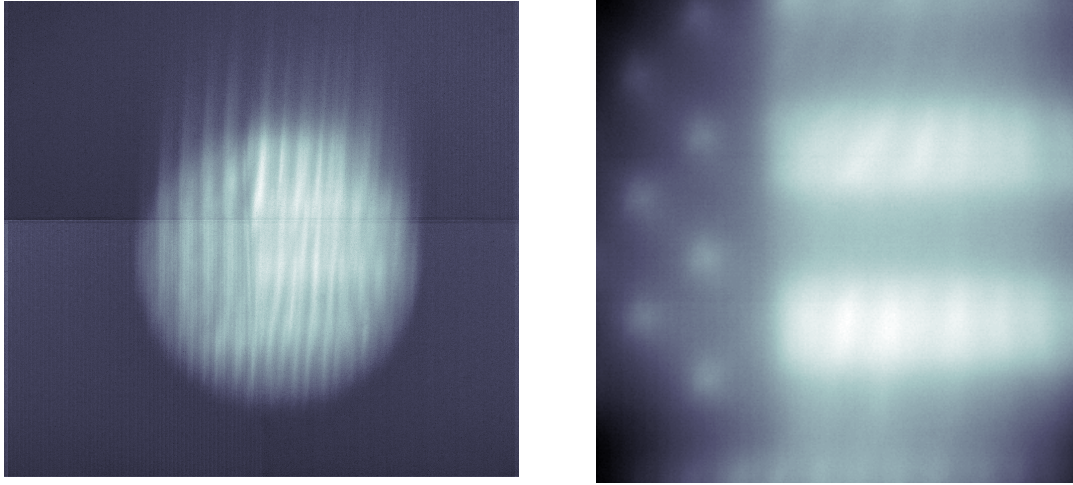


Figure 39. Reconstructed intensity images in 10nm increments for a Hg point-like source ranging from 440 to 550 nm.



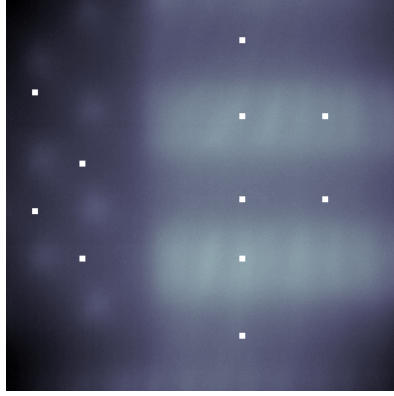
(a) Unprocessed image

(b) Reconstructed image

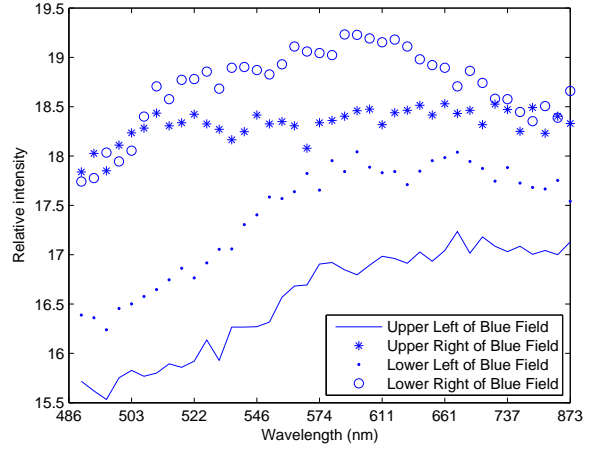
Figure 40. Image (a) is an unprocessed image of an American flag as seen through the imager. Image(b) is the reconstructed intensity image of multiple wavelengths “added” together.

from wavelengths 486 nm to 873 nm. The plots were created using a pixel deviation algorithm as opposed to a wavelength shift. Therefore, the bottom axes of plots are not uniformly spaced. The constant pixel deviation was selected because of the non-linearity of the dispersion of the DVP, as shown in Figure 10. To further highlight this fact, Tables 4 and 5 show specific sample spaces used in reconstruction. As the wavelengths increase, the pixel separation decreases from a couple of pixels per nm of wavelength to sub pixel intervals. However, for completeness, a plot of flag spectra in constant incremental wavelength is also provided in Figure 42. The pixel locations utilized for the spectra reconstruction were selected to compare the various colors of the flag and to provide insight to how the intensity was effected at the differing locations. The blue field will be the first portion of the flag to be discussed.

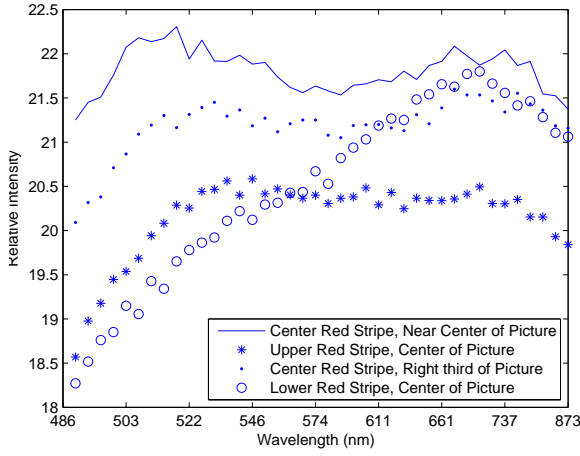
The first correlation one can draw from the intensity plot is how the intensity of the blue field decreases as the pixels move from the center of the image, to the left



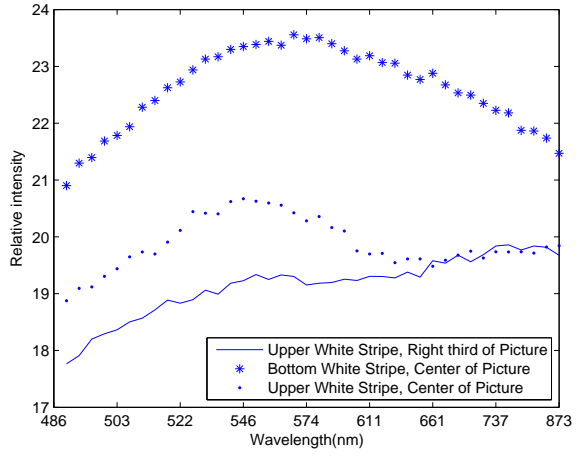
(a) Reconstructed flag



(b) Blue field



(c) Red stripe



(d) White stripe

Figure 41. Image (a) is the reconstructed intensity image of multiple wavelengths of an American flag. The white squares on the image represent the different locations of pixels chosen for the intensity plots. Plot (b) shows the intensity of four pixel locations on the blue field. Plot (c) is the intensity of four pixel locations on red stripes of the flag. Plot (d) shows the intensity of three pixel locations on white stripes of the flag.

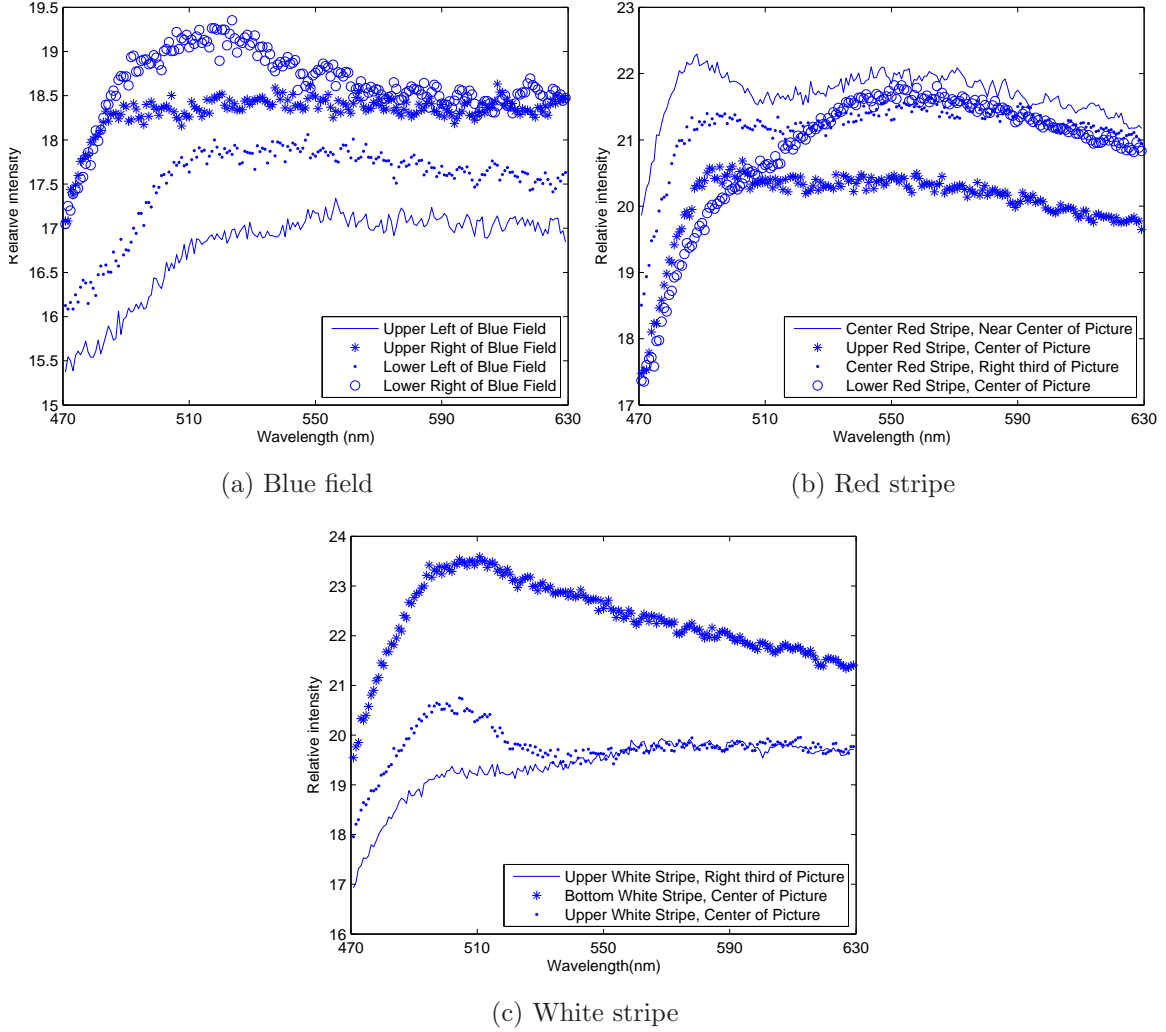


Figure 42. Plots in (a) are the intensity plots of the blue field pixels plotted in incremental wavelength dispersion. Plots in (b) are the intensity plots of the red stripe pixels plotted in incremental wavelength dispersion. Plots in (c) are the intensity plots of the white stripe pixels plotted in incremental wavelength dispersion.

Table 4. Wavelength dispersion in constant pixel increments.

Pixel Displacement	Wavelength (nm)
-290	400
-250	411
-200	428
-150	447
-100	471
-50	503
0	548
50	611
100	737

Table 5. Pixel displacement in constant wavelength increments.

Wavelength (nm)	Pixel Displacement
400	-290
450	-144
500	-54
550	4
600	43
650	70
700	89
750	103
800	113
850	121
900	128

and in the upper half of the image. The reason why the intensity decreases as the pixels move from the center outward may be due to vignetting. One possible cause of this is because the field stop of the system may not be placed precisely at the focal length of the telescope. Another possibility is that the lenses in the optical train may have some tilt to them.

A possible explanation for the intensity being higher in the lower half of the frame when compared to the upper half of the frame is that the camera had been in operation for a long period of time resulting in higher intensities in the bottom half of the FPA. This increase in intensity is likely due to the camera not being able to cool its detector array effectively when used over an extended period.

The spectrum of the blue field is somewhat puzzling. It is expected that the intensity plot of the blue field would be highest for wavelengths falling within the blue region of the visible spectrum of approximately 500 nm and below. However, in all four cases the spectrum is higher in wavelengths above 500 nm. This is possibly due to the camera's response for wavelengths of 500 nm and below, as illustrated in Figure 13.

The spectrum in each pixel location, to include those in the red and white stripes, may possess artifacts from off-wavelength signals. These artifacts stem from the shift and add algorithm.

The trend lines for the right pixels also correspond fairly well to each other. However, there does not seem to be a strong correlation between the two sets. This could possibly be once again attributed to vignetting. The spectrum for the red stripes draw some similar and some different conclusions as those for the blue field.

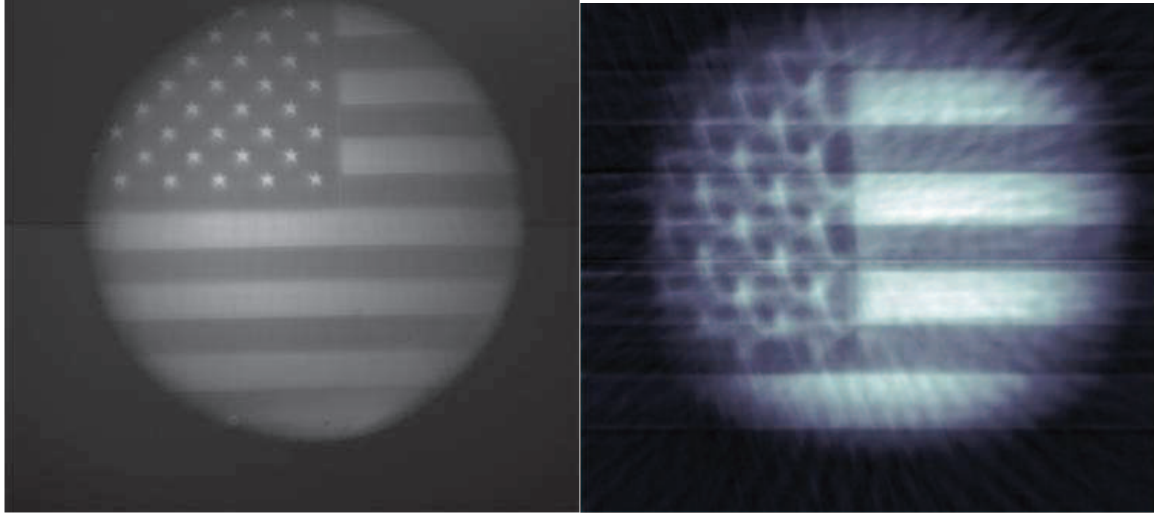
The red stripes intensity once again shows a higher intensity for those pixels located nearer the center than those near the edges of the image. There is a strong correlation in three of the four trend lines for the red stripe. The other plot's differing

trend line may be due to vignetting from its location near the edge. Once again, the bottom half of the image produced red stripe pixels that had higher intensities. Unlike the blue field, the spectrum of the red stripe appears highest, as expected, in wavelengths longer than 600 nm, but also unexpectedly, in lower wavelengths of approximately 500 to 522 nm. It is possible the dye used in the red stripes of the flag possessed some “blue” tones. The red stripes did have intensity levels that were typically higher than the blue field and therefore it could be that the red stripe was a stronger emitter. However, the strongest emitter of the differing colors was the white stripes.

The highest intensity value for the white stripes was from the pixel located in the bottom half of the frame. Two of the trend lines for the white stripe corresponded well, while the third was probably affected by vignetting. The spectral plot for the white stripes for these two trend lines match fairly well with the camera’s response curve.

Bostick constructed a data cube from the same raw data of the American flag. For his reconstruction, Bostick utilized a back projection algorithm that he created [3] and took into account the errors introduced by the possible motor mount misalignment and the unbalanced motor. A picture of the flag taken through the system without the prism and an intensity reconstruction image he created can be seen in Figure 43. The vignetting previously discussed can be seen in the left picture of Figure 43. The Bostick intensity picture has higher spatial contrast than the intensity picture created without error correction.

Figure 44 is an image and a series of intensity plots from the data cube Bostick created. The upper left image is an image of one spectral bin in the data cube. The dark squares on the image represents the different locations that pixels were chosen for the spectral plots. The upper right plot shows the intensity of pixel locations



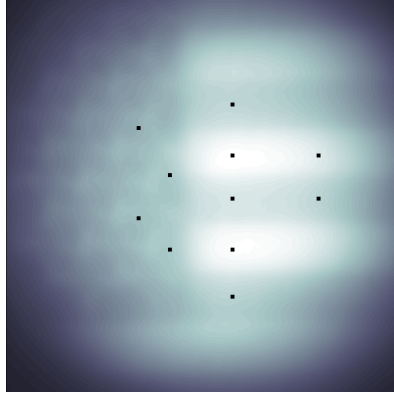
(a) Picture of flag

(b) Bostick's reconstructed flag

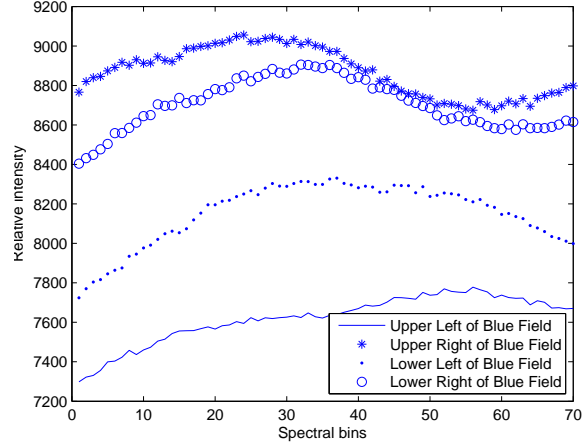
Figure 43. Image (a) is a picture of the flag taken through the imager without the prism in place. The image (b) is a reconstructed intensity image of the flag created by Bostick.

on the blue field. The lower left plot shows the intensity of pixel locations on red stripes of the flag. The lower right plot shows the intensity of pixel locations on white stripes of the flag. Trends for the pixel intensity plots for the Bostick data cube tend to have a stronger correlation than trend lines previously discussed. The error correction conducted during reconstruction resulted in spectral data that possessed fewer artifacts.

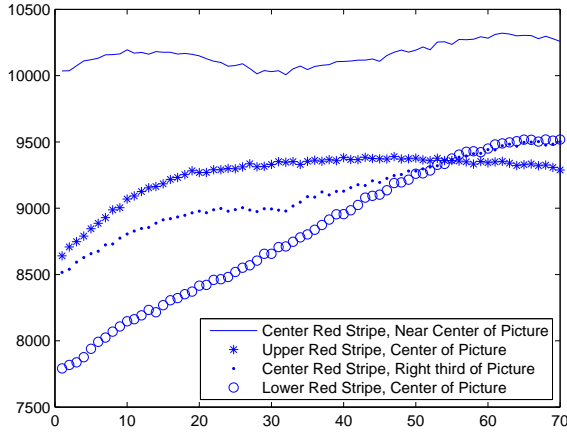
Although this sort of manual error correction for all collected data would ideally occur for reconstruction, this was not done in the rest of the research. A spectral source with strong emission, when compared to the rest of the scene, was not available for subsequent testing and manual error correction is a time intensive process. Furthermore, a reference spectrometer would have ideally been utilized to compare/validate the results of the instrument. Unfortunately, due to the limitations of the available equipment, this was not possible. The subsequent reconstructions without error correction, although not spatially or spectrally perfect, do illustrate the



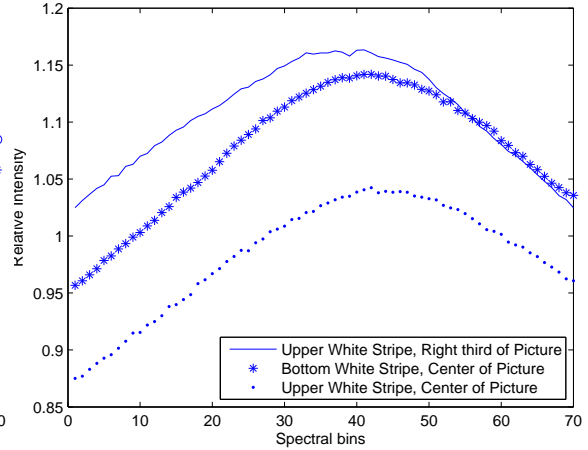
(a) Reconstructed flag



(b) Blue field



(c) Red stripe



(d) White stripe

Figure 44. These series of images are based upon a data cube that Bostick created utilizing the same raw data that was used in the earlier reconstruction. Image (a) is an image of one bin in the data cube. The dark squares on the image represent the different locations of pixels chosen for the intensity plots. Plot (b) shows the intensity of pixel locations on the blue field. Plot (c) shows the intensity of pixel locations on red stripes of the flag. Plot (d) shows the intensity of pixel locations on white stripes of the flag.

potential the imager possess.

5.3 Transient Event Reconstruction

Lastly, a series of transient events were recorded outdoors in the late afternoon at a range of approximately 135 m. The initial test was a firecracker explosion that occurred in front of a Hg pen lamp housed in a cardboard box painted black. The goal of the test was to illustrate how the imager could reconstruct a scene when a transient event occurred during the collection period. Unlike traditional hyperspectral imagers, if a scene change occurs during CT instrument collection, spectral and spatial data can still be processed utilizing reconstruction algorithms.

Figure 45 displays three unprocessed frames of a collection that occurred over one prism rotation. The entire collection period was approximately 0.12 s. The left frame is captured just prior to the transient event, a firecracker exploding. The middle frame is the first frame of the firecracker exploding. The right frame is an image where the effects of the transient event has dissipated. To reconstruct the Hg pen lamp and the extended broad spectrum scene of the box and the background, the data with the transient event was not used in the reconstruction processing. Instead only half of the captured data, i.e. frames for only one half of a prism rotation, was utilized in the reconstruction. The pen lamp was the first element reconstructed in the scene.

The Hg pen lamp was placed in the scene so the effectiveness of the reconstruction could be illustrated against a target with high spectral contrast. In order to provide it protection from the explosion, the pen lamp was placed in the cardboard box. The cardboard box was also utilized to reduce the amount of stray light reflections that could occur off of the pen lamp apparatus. A side benefit of utilizing the cardboard box was to illustrate how a broad spectrum portion of the scene could also be recon-

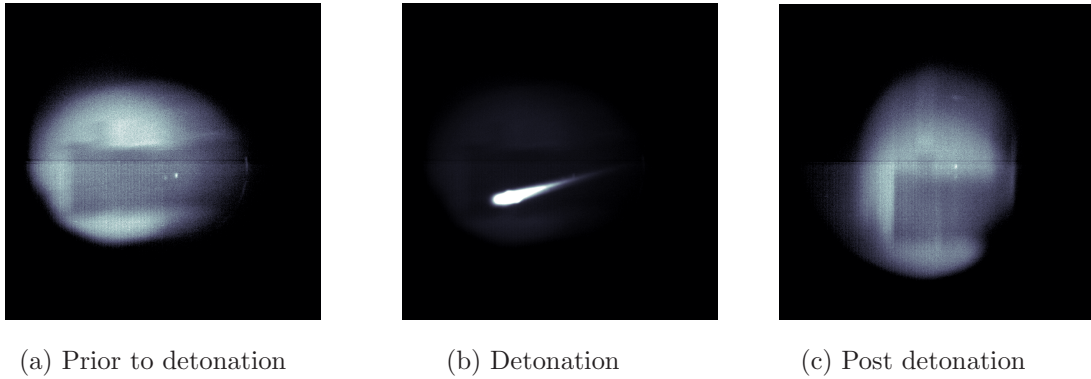


Figure 45. These images are a series of unprocessed images from a transient event test. Image (a) is a scene prior to detonation. Image (b) is a scene as the explosion occurs. Image (c) is the scene after the effects of the explosion have dissipated.

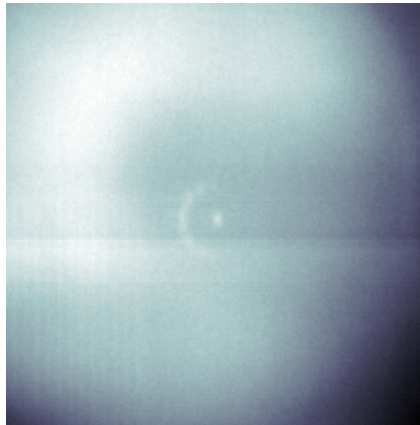


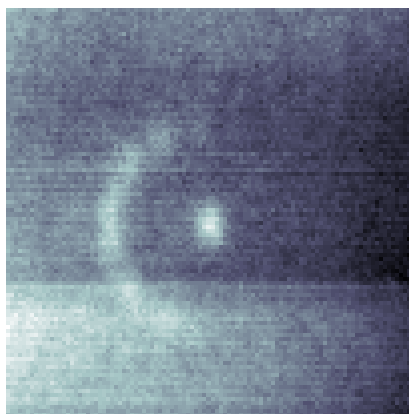
Figure 46. The reconstructed image at 568 nm of a Hg pen lamp in an extended broad spectrum scene after transient event. Note in the reconstruction the semi-circular artifact of an off-wavelength emission line.

structed. Figure 46 is an example of the entire scene reconstruction at a particular wavelength; in this case an Hg emission line of 568 nm. Note in the reconstruction the semi-circular artifact of an off-wavelength emission line. Other Hg emission lines were also reconstructed. Figure 47 displays the emission lines of 568, 546, and 436 nm at a close up view. The Hg pen lamp was a relatively weak emitter compared to the background illumination from the late afternoon sun. Because of this fact, the reconstruction intensity appears faded out in the images.

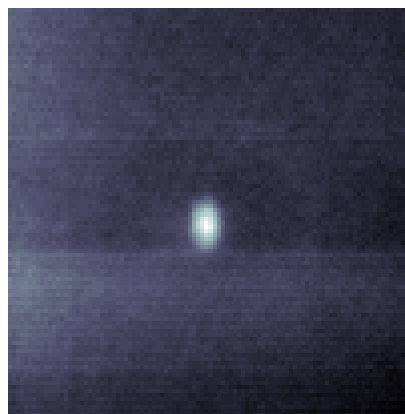
Figure 48 displays an indoor color photo of the box that housed the Hg pen lamp and a reconstructed image of the box. Image reconstruction of the box was not the primary purpose of the experiment. However, it does illustrate that reconstruction of a scene can be accomplished fairly well with data from only half a prism rotation. Image quality of the box would probably be improved with a more sophisticated reconstruction algorithm. Spatial image reconstruction of the transient event was not possible because the scene evolved in each frame imaged. However, spectral reconstruction could occur for the explosion if the center point of dispersion is known for the firecracker.

Figure 49 displays a frame taken during the explosion and a notional spectrum of the explosion for the frame. The entire explosion lasted approximately 0.01 s. Because the center point of dispersion was unknown for this frame the intensity plot in Figure 49 does not have any wavelengths assigned to it. It is possible that a potassium emission line is present. There is at least one spectral feature that is easily located due to the relatively high intensity when compared to the rest of the spectrum. A strong potassium emission line is frequently observed in explosive events as potassium is a common contaminant found in explosives. If other spectral features can be identified, then the entire spectral characteristics of the scene can be determined.

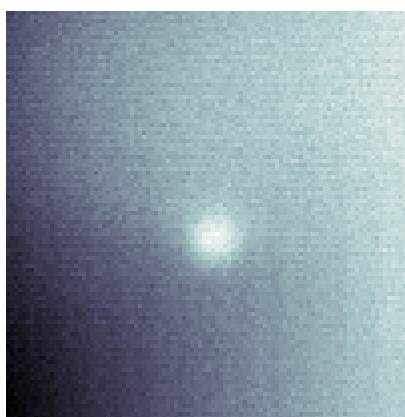
A second firecracker test occurred which allowed the center point of dispersion to



(a) Hg 568 nm



(b) Hg 546 nm

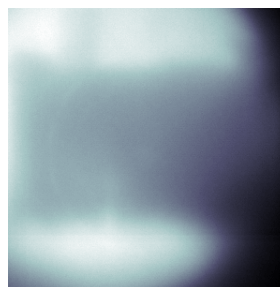


(c) Hg 436 nm

Figure 47. Reconstructed spectral images of the pen lamp at (a) 568 nm, (b) 546 nm, and (c) 436 nm.



(a)



(b)

Figure 48. Image (a) is a color picture of the box that housed the Hg pen light. Image (b) is a reconstructed image of the box.

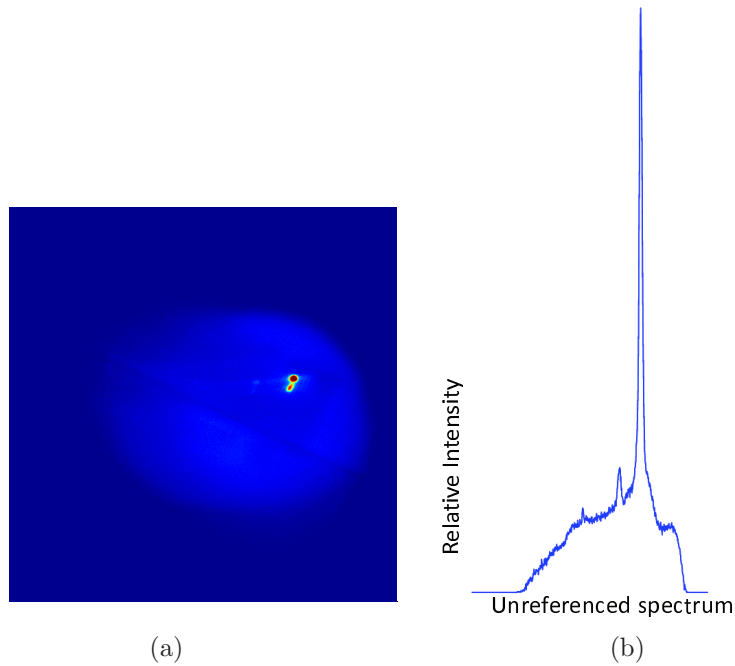


Figure 49. Intensity image (a) of the explosion with an unreferenced spectral plot (b) of a firecracker detonation.

be determined. For the test, a firecracker was held in place by a mount. A portion of the firecracker caught fire and remained in place after the explosion. Imagery of the remnant fire for a quarter rotation of the prism was captured and allowed the center point to be located. Figure 51 displays the spectrum of four different frames of the explosion. The first frame, taken at approximately 0.001 s after the explosion, shows a broad spectral feature centered at 795 nm. This feature could be the potassium emission line of 766 nm. The small “bump” near 600 nm in the same plot could be a sodium emission line. Sodium, which emits at 589 nm, is also a common spectral feature found in explosive events. The observed peaks are much wider than atomic transition lines, but the width may be due to finite spatial extent of the source and known aberrations in the system. Because of the known aberrations and the spectral response of the camera, the wavelength axis in Figure 51 was restricted to the visible portion of the spectrum, 400-900 nm. The second frame, taken at approximately

0.002 s after the explosion, once again has two emission lines present and could be correlated to those spectral features previously mentioned. The third frame, taken at approximately 0.003 s after the explosion, shows a broadband emission, consistent with blackbody radiation, with some absorption occurring near 600 nm. An oxygen absorption band exists in this same region. However, the absorption could also be attributed to byproducts of the combustion process the explosion created. Frame four, taken approximately 0.004 s after the explosion, once again highlights the absorption that occurs near 600 nm.

Utilizing the frames in Figure 51, and the next frame in the movie, approximately 0.005 s after the explosion, the intensity of these emission and absorption features were compared to the intensity of the broadband thermal emission in Figure 52. To derive these plots, a fit of the data excluding the potential emission or absorption regions was created, labeled as I_{Fit} in the plot. The emission above or the absorption below the fit was then divided by the intensity of the fit data for the band of interest.

The spectral intensity of the four frames in Figure 51, plotted on a single frame, illustrate the evolution of intensity of spectral plots over time. Figure 51b, allows a finer look of the spectral evolution without the high intensity frame one, Figure 51a.

Figure 50 was created to highlight how the relative intensity of the explosion and resulting fire diminishes over time. To create these plots, more frames of the captured movie was utilized than those in Figure 51, and was created by summing a number of rows over the entire spectrum. Note at approximately 0.009 s, the intensity begins to increase once again after falling. The increase is due to the firecracker housing catching fire. In Figure 50 the highest intensity occurs one time step after the explosion, which is likely due to the concentration of the blast during the first frame of the explosion. This plot coupled with the first set of firecracker test illustrates the capability of the imager to capture and reconstruct spectrum for transient events

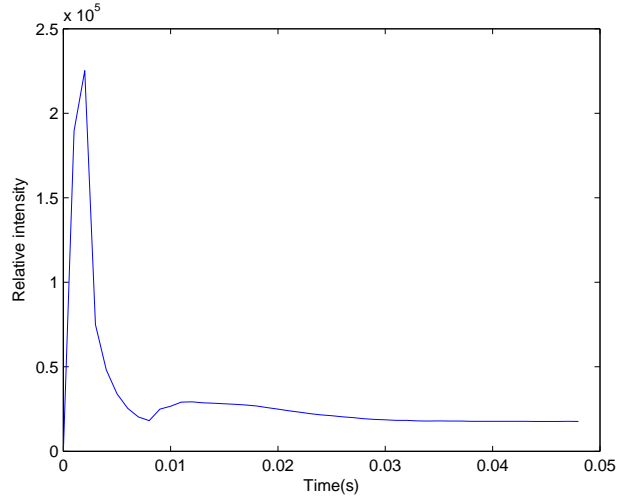
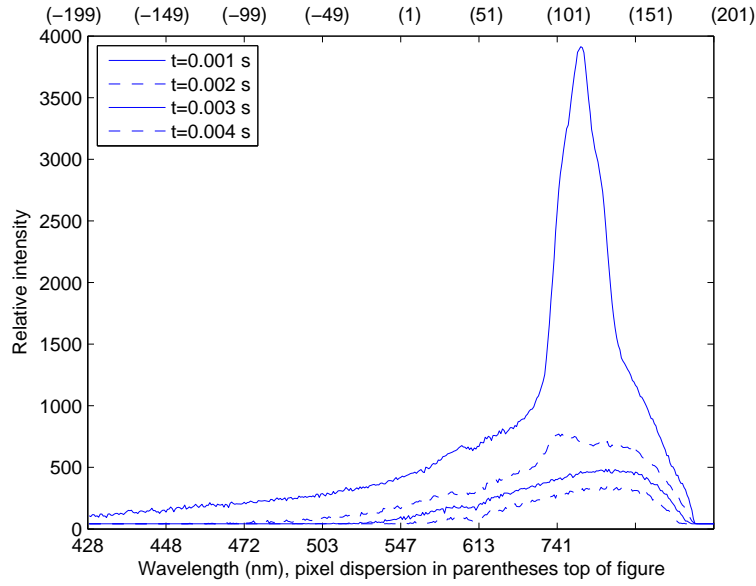


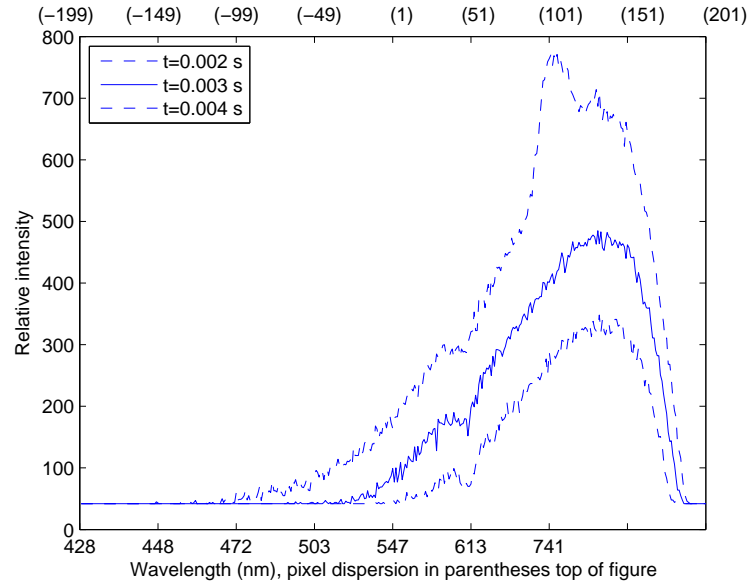
Figure 50. This plot highlights how the relative intensity of the explosion and the resulting fire diminishes over time. Note at approximately 0.009 s, the intensity begins to increase once again after falling. The increase is due to the firecracker housing catching fire.

as well as utilize data after or prior to the transient event to reconstruct the static portion of the scene.

Finally, Figure 53 illustrates the potential capability of the imager to capture a relatively large spatial scene of a transient event. This image is a single unprocessed frame of a movie taken at night of a “AFIT” sign illuminated by a firecracker explosion. To collect data only of the AFIT sign, an opaque shield was placed between the imager and the firecracker. Because only one AFIT sign is visible in the picture, there was one very strong emission line in the firecracker spectrum. Other emission lines were not strong enough to cause additional clearly visible dispersed AFIT sign images.

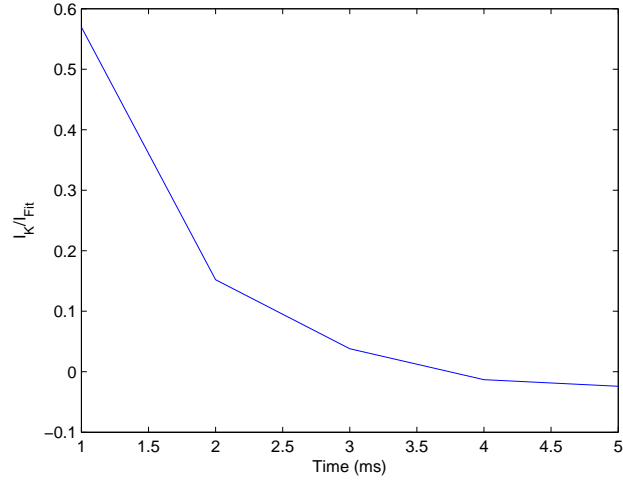


(a) Intensity plots of $t=0.001$ to 0.004 s

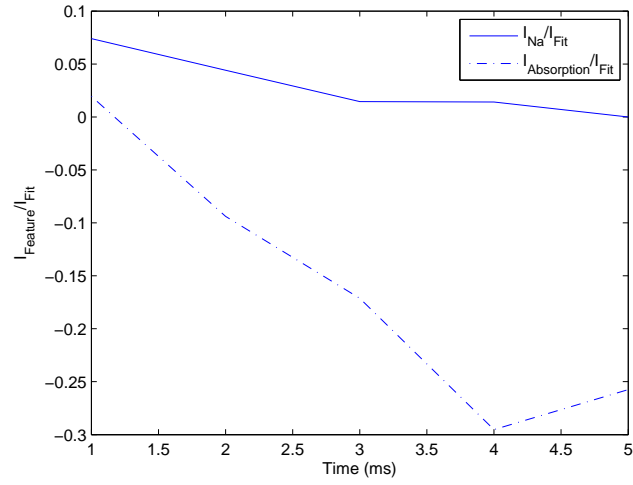


(b) Intensity plots of $t=0.002$ to 0.004 s

Figure 51. These plots highlight how the relative intensity of the plots across the spectrum is decreasing. Plots in (a) are the different relative intensity plots of the explosion starting from $t=0.001$ to 0.004 s. Plots in (b) are the different relative intensity plots of the explosion starting from $t=0.002$ to 0.004 s. Limiting the time to only $t=0.002$ to 0.004 s in plot (b) allows a finer look at the spectrum without the high intensity of $t=0.001$ s.



(a) Potassium intensity



(b) Sodium and Absorption intensity

Figure 52. Intensity plots of potassium, sodium, and absorption bands. The signal for each band was divided by the intensity of the band fit. Plot (a) is the ratio of the potassium band. Plot (b) has the sodium band ratio and the absorption band ratio graphed.

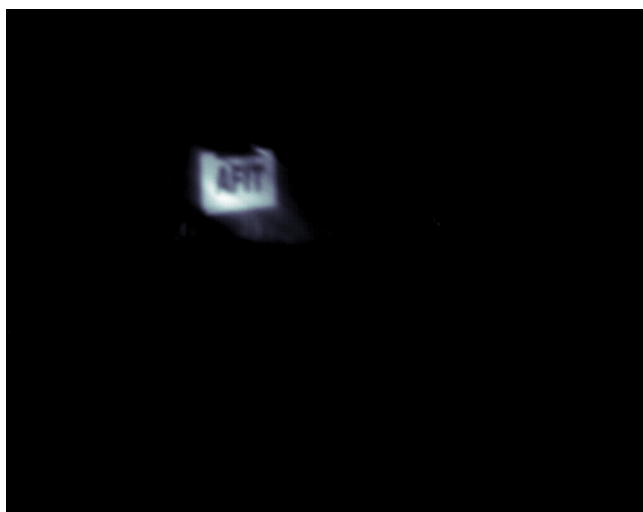


Figure 53. An AFIT sign illuminated by an explosion.

VI. Conclusions and Recommendations

This research is focused on the construction and characterization of a CT imager. The instrument is currently the fastest known direct vision prism hyperspectral CT imager. The imager was capable of acquiring spectral data for a transient event lasting less than 0.12 s. The ability to identify potassium, sodium, and absorption features shows the potential this instrument possess. This research has shown that the instrument has the ability to capture data of static scenes, and more importantly, the imager acquired spectral data for rapidly evolving scenes. The same data of firecracker detonations from which the spectrum was extracted was also utilized to reconstruct spectral and spatial data for the non-transient portions. The ability to recreate spatial and spectral data of a scene in which an explosion occurs during collection is an advantage over traditional hyperspectral imagers. The research also illustrates the errors introduced into data reconstruction when there is component misalignment. It was also shown that knowledge of precise prism angular position during framing is integral to achieving the best reconstruction results. Finally, the use of a simple “shift and add” algorithm proved useful in the testing and characterization of the instrument. However, an algorithm that removes scene artifacts and reduces the amount of error associated with estimates, such as the location of the center of dispersion, would create results with more confidence and better spectral and spatial resolution.

Modifications to the instrument have already taken place. An encoder and a new motor have been replaced the motor/encoder utilized in this research. With the new motor, data acquisition can increase to approximately 100 Hz prism rotation rate; however acquiring data at this rate will result in reduced camera resolution. Other improvements to the current system that are being explored include acquiring a new DVP that provides better dispersion at longer wavelengths, securely fixing all

components to avoid optical misalignment, and reducing the size and weight of the instrument for better deployability.

Future research should continue on the acquisition and reconstruction of transient events. A reference spectrometer will assist in the calibration/validation of the instrument and the reconstruction algorithm. Of particular interest will be the ability to reconstruct both the spatial and spectral features of a transient scene.

Bibliography

- [1] An, M., A. Brodzik, J. Mooney, and R. Tolimieri. “Data Restoration in Chromotomographic Hyperspectral Imaging”. *Proceedings of SPIE*, 4123, 2000.
- [2] Book, Todd A. *Design Analysis of a Space-Based Chromotomographic Imaging Experiment*. Master’s thesis, Air Force Institute of Technology, Wright-Patterson AFB, March 2010.
- [3] Bostick, R.L. and G.P. Perram. “Hyperspectral Imaging Using Chromotomography: A Fieldable Visible Instrument for Transient Events”. *International Journal of High Speed Electronics and Systems*, 18(3), Sep. 2008.
- [4] Bostick, R.L., G.P. Perram, and R. Tuttle. “Characterization of Spatial and Spectral Resolution of a Rotating Prism Chromotomographic Hyperspectral Imager”. *Proceedings of SPIE*, 7319, Apr. 2009.
- [5] Bostick, R.L., G.P. Perram, and R. Tuttle. “Instrumental Systematic Errors in a Chromotomographic Hyperspectral Imaging System”. *IEEE*, pending publication 2010.
- [6] Brodzik, A.K. and J.M. Mooney. “Convex Projections Algorithm for Restoration of Limited-angle Chromotomographic Images”. *Journal of the Optical Society of America*, 26(2), Feb. 1999.
- [7] Brooks, R. and G. Di Chiro. “Principles of Computer Assisted Tomography (CAT) in Radiographic and Radioisotopic Imaging”. *Physics and Medicine and Biology*, 21(5), 1976.
- [8] Campbell, J. B. *Introduction to Remote Sensing*. The Guilford Press, New York, 2007.
- [9] Chabay, R. and B. Sherwood. *Matters and Interactions*. John Wiley and Sons, New York, 2002.
- [10] Chen, Y., J. Lo, J. Baker, and J. Dobbins III. “Gaussian Frequency Blending Algorithm with Matrix Inversion Tomosynthesis (MITS) and Filtered Back Projection (FBP) for Better Digital Breast Tomosynthesis Reconstruction”. *Proceedings of SPIE*, 6142, 2006.
- [11] Chen, Y., J. Lo, and J. Dobbins III. “Impulse Response Analysis for Several Digital Tomosynthesis Mammography Reconstruction Algorithms”. *Proceedings of SPIE*, 5745, 2005.
- [12] Deming, R. “Chromotomography for a Rotating-Prism Instrument Using Back-projection, then Filtering”. *Optics Letter*, 31(15), Aug. 2006.

- [13] Descour, M. R. and E. L. Dereniak. “Computed-Tomography Imaging Spectrometer: Experimental Calibration and Reconstruction Results”. *Applied Optics*, 34(22), Aug. 1995.
- [14] Descour, M. R., C. E. Volin, E. L. Ereniak, K. J. Thome, A. B. Schumacher, D. W. Wilson, and P. D. Maker. “Demonstration of a High Speed Non-scanning Imaging Spectrometer”. *SPIE*, 3379, Apr. 1998.
- [15] Eismann, M. T. *Hyperspectral Remote Sensing*. Unpublished, Dayton, OH, 2006.
- [16] Ford, B., J. Salazar, and M. Wilson. *Reconstruction Algorithm Development and Assessment for a Computed Tomography Based-Spectral Imager*. Sandia Report, SAND2005-6385, Albuquerque, NM, Oct. 2005.
- [17] Gat, N., G. Scriven, M.D. Li, and J. Zhang. “Development of Four-Dimensional Imaging Spectrometers 4D – IS”. *Proceedings of SPIE*, 6302, 2006.
- [18] Gould, M. and S. Cain. “Development of a Fast Chromotomographic Spectrometer”. *Optical Engineering*, 44(11), Nov. 2005.
- [19] Gould, Malcolm G. *Reconstruction of Chromotomographic Imaging System Infrared Hyperspectral Scenes*. Master’s thesis, Air Force Institute of Technology, Wright-Patterson AFB, March 2005.
- [20] Gustke, Kevin C. *Reconstruction Algorithm Characterization and Performance Monitoring in Limited-Angle Chromotomography*. Master’s thesis, Air Force Institute of Technology, Wright-Patterson AFB, March 2004.
- [21] Hecht, E. *Optics*. Pearson, San Francisco, 2002.
- [22] Laboratory, NASA/Jet Propulsion. “AVIRIS Moffett Field Image Cube. Technical report”. URL <http://aviris.jpl.nasa.gov/html/aviris.cube.html>., 2007.
- [23] LeMaster, Daniel A. *Design and Model Verification of an Infrared Chromotomographic Imaging System*. Master’s thesis, Air Force Institute of Technology, Wright-Patterson AFB, Decemeber 2004.
- [24] Mantravadi, S. “Spatial and Spectral Resolution Limits of Hyperspectral Imager Using Computed Tomography: A Comparison”. *Aerospace Conference, 2007 IEEE*, 4028, 2007.
- [25] Mooney, J., A.K. Brodzik, and M. An. “Principal Component Analysis in Limited-Angle Chromotomography”. *Proceedings of SPIE*, 3118, 1997.
- [26] Mooney, J. M. and W. S. Ewing. “Characterization of a Hyperspectral Imager”. *IRIS Proceedings on CD-ROM*, 1998.

- [27] Mooney, J. M., V. E. Vickers, M. An, and A. K. Brodzik. “High-Throughput Hyperspectral Infrared Camera”. *Optical Society of America, A*, 14(11), Nov. 1997.
- [28] Murguia, J., T.E. Reeves, J.M. Mooney, W.S. Ewing, F.D. Shepherd, and A.K. Brodzik. “A Compact Visible/Near Infrared Hyperspectral Imager”. *Proceedings of SPIE*, 4028, Mar. 2000.
- [29] Orson, J.A., W.F. Bagby, and G.P. Perram. “Hyperspectral Infrared Signatures for Bomb Detonations”. *Infrared Physics and Technology*, 44, Jun. 2002.
- [30] Research, Vision. URL <http://www.visionresearch.com/>, 2010.
- [31] Sheirich, Phillip A. *An Engineering Trade Space Analysis for a Space-Based Hyperspectral Chromotomographic Scanner*. Master’s thesis, Air Force Institute of Technology, Wright-Patterson AFB, March 2009.
- [32] Shepherd, F., J.M. Mooney, T.E. Reeves, and P. Dumont. “Adaptive MWIR Spectral Imaging Sensor”. *Proceedings of SPIE*, 7055, Aug. 2008.
- [33] Shepherd, F., J.M. Mooney, T.E. Reeves, D.S. Franco, J.E. Murguia, C. Wong, P. Dumont, F. Khaghani, and G. Diaz. “SWIR Variable Dispersion Spectral Imaging Sensor”. *Proceedings of SPIE*, 6660, Sep. 2007.
- [34] Wagadarikar, A., N.P. Pitsianis, X. Sun, and D.J. Brady. “Video Rate Spectral Imaging Using a Coded Aperture Snapshot Spectral Imager”. *Optics Express*, 17(8), Apr. 2009.
- [35] Wolfe, W. L. *Introduction to Imaging Spectrometers*. SPIE Optical Engineering Press, Bellingham, Washington, 1997.

REPORT DOCUMENTATION PAGE

Form Approved
OMB No. 0704-0188

The public reporting burden for this collection of information is estimated to average 1 hour per response, including the time for reviewing instructions, searching existing data sources, gathering and maintaining the data needed, and completing and reviewing the collection of information. Send comments regarding this burden estimate or any other aspect of this collection of information, including suggestions for reducing this burden to Department of Defense, Washington Headquarters Services, Directorate for Information Operations and Reports (0704-0188), 1215 Jefferson Davis Highway, Suite 1204, Arlington, VA 22202-4302. Respondents should be aware that notwithstanding any other provision of law, no person shall be subject to any penalty for failing to comply with a collection of information if it does not display a currently valid OMB control number. **PLEASE DO NOT RETURN YOUR FORM TO THE ABOVE ADDRESS.**

1. REPORT DATE (DD-MM-YYYY) 27-03-2010			2. REPORT TYPE Master's Thesis		3. DATES COVERED (From — To) Aug 2008 — Mar 2010	
4. TITLE AND SUBTITLE Development and Demonstration of a Field-Deployable fast Chromotomographic Imager					5a. CONTRACT NUMBER	
					5b. GRANT NUMBER	
					5c. PROGRAM ELEMENT NUMBER	
6. AUTHOR(S) O'Dell, Daniel C., Capt, USAF					5d. PROJECT NUMBER	
					5e. TASK NUMBER	
					5f. WORK UNIT NUMBER	
7. PERFORMING ORGANIZATION NAME(S) AND ADDRESS(ES) Air Force Institute of Technology Graduate School of Engineering and Management (AFIT/EN) 2950 Hobson Way WPAFB OH 45433-7765					8. PERFORMING ORGANIZATION REPORT NUMBER AFIT/GEO/ENP/10-M01	
9. SPONSORING / MONITORING AGENCY NAME(S) AND ADDRESS(ES) Withheld					10. SPONSOR/MONITOR'S ACRONYM(S)	
					11. SPONSOR/MONITOR'S REPORT NUMBER(S)	
12. DISTRIBUTION / AVAILABILITY STATEMENT APPROVED FOR PUBLIC RELEASE; DISTRIBUTION UNLIMITED.						
13. SUPPLEMENTARY NOTES						
14. ABSTRACT A field deployable hyperspectral imager utilizing chromotomography (CT), with a direct vision prism (DVP) as the dispersive element, has been constructed at AFIT. This research is focused on the construction and characterization of a CT imager as prototype for a follow on International Space Station based instrument. The instrument is currently the fastest known direct vision prism hyperspectral CT imager. The imager was capable of acquiring spectral data for a transient event lasting less than 0.12 s. The ability to identify potassium, sodium, and absorption features from the instrument's acquired data shows the potential this imager possess. This research has shown that the instrument has the ability to capture data of static scenes, and more importantly, the imager acquired spectral data for rapidly evolving scenes. Because CT imaging has the potential ability to capture spatial and spectral data from transient events, a space-based system may enhance current capabilities of identifying, classifying, and characterizing battlespace events such as artillery/AAA muzzle flashes, detonations, and missile launches.						
15. SUBJECT TERMS Hyperspectral, chromotomography, direct vision prism, CTE _x						
16. SECURITY CLASSIFICATION OF:			17. LIMITATION OF ABSTRACT	18. NUMBER OF PAGES	19a. NAME OF RESPONSIBLE PERSON	
a. REPORT	b. ABSTRACT	c. THIS PAGE			Lt Col Michael R. Hawks	
U	U	U	UU	91	19b. TELEPHONE NUMBER (include area code) (937) 255-3636, x4828; mhawks@afit.edu	